Atmos. Chem. Phys., 26, 15423–15443, 2026
https://doi.org/10.5194/acp-26-15423-2026
© Author(s) 2026. This work is distributed under
the Creative Commons Attribution 4.0 License.

Atmospheric Chemistry and Physics
Open Access
EGU

Research article

Retrieval of ultraviolet aerosol absorption from radiation measurements in young wildfire plumes

Jan-Lukas Tirpitz[1,a], Nathaniel Brockway[1,b], Santo Fedele Colosimo[1], Robert Spurr[2], Matt Christi[3], Samuel Hall[4], Kirk Ullmann[4], Vijay Natraj[8], Nicolas Theys[9], Johnathan Hair[5], Taylor Shingler[5], Rodney Weber[6], Ruchen Zhu[6], Jack Dibb[7], Richard Moore[5], Elizabeth Wiggins[5], and Jochen Stutz[1]

[1]Department of Atmospheric and Oceanic Sciences, UCLA, Los Angeles, CA, USA
[2]RT Solutions Inc., Cambridge, MA, USA
[3]independent researcher: Fort Collins, CO 80524, USA
[4]National Center for Atmospheric Research, Atmospheric Chemistry Observations and Modeling Laboratory, Boulder, Colorado, USA
[5]National Aeronautics and Space Administration, Langley Research Center, Hampton, Virginia, USA
[6]School of Earth and Atmospheric Sciences, Georgia Institute of Technology, Atlanta, GA, USA
[7]Earth Systems Research Center, University of New Hampshire, Durham, NH, USA
[8]Jet Propulsion Laboratory, California Institute of Technology, Pasadena, CA, USA
[9]Royal Belgian Institute for Space Aeronomy, Brussels, Belgium
[a]now at: Department of Chemistry, CU-Boulder, Boulder, CO, USA
[b]now at: Southcoast Air Quality Management District, CA, USA

Correspondence: Jan-Lukas Tirpitz (jltirpitz@gmail.com) and Jochen Stutz (jochen@atmos.ucla.edu)

Received: 8 November 2025 – Discussion started: 5 February 2026
Revised: 28 September 2026 – Accepted: 2 October 2026 – Published: 3 November 2026

Abstract. Aerosols play an important role for atmospheric radiative transfer in biomass burning (BB) plumes, where they control photochemistry, direct radiative forcing, and radiation-induced atmospheric dynamics. The optical properties of BB aerosol, however, remain poorly constrained with respect to their absorptive properties at ultraviolet and visible wavelengths. Aircraft-based observations show considerable variability due to heterogeneity in BB plumes, and different measurement methods do not agree with each other. To overcome this challenge, we have developed an algorithm based on the VLIDORT for photochemistry (VPC) radiative transfer model to retrieve the imaginary refractive index $k(\lambda)$ from airborne actinic flux observations at wavelengths λ of 308–440 nm. Using three flights from NASA/NOAA's Fire Influence on Regional to Global Environments and Air Quality (FIREX-AQ) airborne experiment, we obtain values $k(387\,\text{nm})$ between 0.02 and 0.03, and absorption Angstrom exponents α_k between 3 and 5 for different transects. Volume absorption cross section (VAC) and single scattering albedo generally agree with aircraft-based observations, but show less variability, most likely because of the inherent spatial averaging of our observations. $k(\lambda)$, VAC and single-scattering co-albedo decrease with physical plume age, with half-lives $\tau_{1/2}$ of 13 ± 3, 16 ± 4 and 17 ± 4 h, respectively. Based on our observations, we present a parameterization of the absorptive properties of BB aerosol from western US wildfires as a function of wavelength and plume age, which will help to improve the representation of BB aerosol in models.

Published by Copernicus Publications on behalf of the European Geosciences Union.

1 Introduction

The optical properties of biomass burning (BB) aerosols in the ultraviolet (UV) and visible (Vis) spectral range play an important role in quantifying the impact of BB emissions on climate and air quality. These properties control plume radiative transfer, so they are of direct relevance for plume photochemical processing, direct radiative forcing, remote sensing of plume composition, and radiation-induced atmospheric dynamics.

A crucial parameter contributing to these effects is the particle absorptivity and its dependence on the radiation wavelength, λ. It is commonly described via the particle single scattering albedo (SSA), $\omega(\lambda)$, or the imaginary part of the refractive index (RI), $k(\lambda)$, of the particle material, which is directly linked to the single scattering co-albedo (SSC $=1-$ SSA) (Bohren and Huffman, 1998; Moosmüller et al., 2009). UV-Vis particle absorption properties allow us to distinguish four BB particle components: non-absorbing compounds (NAC), black carbon (BC), brown carbon (BrC), and dark brown carbon (d-BrC). NAC compounds possess a negligible imaginary RI and thus only scatter light. They consist of inorganic material, water, and non-absorbing organic compounds. BC refers to refractory elemental carbon, featuring a strong uniform absorption over the UV-Vis spectral range with k on the order of 0.8 (Bond and Bergstrom, 2006). BrC comprises a subgroup of organic compounds, which is weakly absorbing in the visible ($k \approx 0.01$) but shows a strong increase in absorption towards the UV, approaching values of $k \gtrsim 0.1$ at wavelengths $\lambda < 350$ nm (Kirchstetter et al., 2004; Chakrabarty et al., 2014; Laskin et al., 2015). D-BrC was recently proposed as an additional optically relevant compound (Chakrabarty et al., 2023), comprising insoluble organic compounds with similar absorption behaviour as BC but a smaller imaginary RI of $k \approx 0.1$.

Because of their differing RI values, the four classes show very different scattering and absorption properties, as illustrated in Fig. 1A, where absorption, scattering and extinction (absorption + scattering) cross-sections for spherical homogeneous particles of typical size (≈ 100 nm in radius) are shown. The extinction cross-section is controlled by the particle size and the real RI. The latter is similar for the different compounds, and so is their extinction cross-section. In contrast, the balance between scattering and absorption, i.e. the SSA, is determined by the imaginary RI, which varies among the compounds by several orders of magnitude.

In the case of a mixed BB particle of the same diameter (Fig. 1B), BrC typically dominates the optical properties in the UV and short-wave visible, due to its high abundance. Scattering is the dominant process in the visible, making BB plumes act as bright diffusors, similar to clouds (Fig. 1D). Towards the UV, the contribution of absorption increases, rendering the plume relatively dark and opaque (Fig. 1C).

The strong wavelength-dependent UV absorption, imposed by the presence of BrC, constitutes a unique challenge

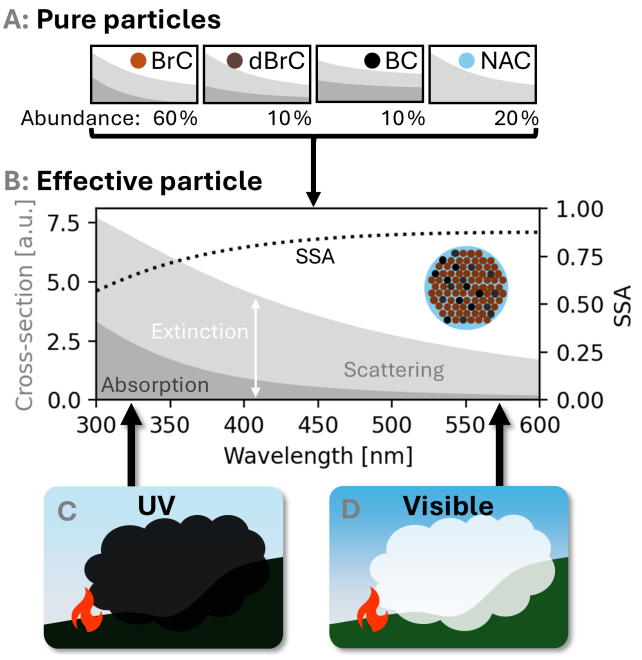


Figure 1. Qualitative illustration of extinction, absorption and scattering cross-sections for a spherical homogeneous particle consisting of various BB particle compounds. Panel **(A)** assumes particles consisting of pure brown carbon (BrC), dark brown carbon (dBrC), black carbon (BC) and non-absorbing compounds (NAC). Panel **(B)** assumes a mixture, based on the abundances of the individual compounds in Panel **(A)**. Abundances are given in terms of volume and represent typical values in a BB plume (Bond et al., 2004; Reid et al., 2005; Sun et al., 2021; Chakrabarty et al., 2023). Panels **(C)** and **(D)** illustrate the macroscopic appearance of a plume consisting of such particles.

for modeling radiative transfer in BB plumes. Among other effects, it influences the plume's direct radiative forcing (Park et al., 2010; Feng et al., 2013; Wang et al., 2014; Liu et al., 2015a; Shamjad et al., 2018; Drugé et al., 2022), it affects the plume photochemical processing (Forrister et al., 2015; Mok et al., 2016; Sumlin et al., 2017; Peng et al., 2021; Xu et al., 2021), limits the sensitivity of satellite measurements (Bousserez, 2014; Theys et al., 2020; Rowe et al., 2022; Theys et al., 2025), and changes atmospheric dynamics by heating the surrounding air (Yu et al., 2002; Barbaro et al., 2014; Hodzic and Duvel, 2018). Despite their importance, BB aerosol absorption properties, particularly in the UV, are still not well constrained, for two major reasons:

First, they vary strongly with aerosol composition and mixing state (Bond et al., 2006), which are both influenced by factors such as fuel composition, fuel moisture content, the combustion process, smoke age, and atmospheric conditions (e.g., Laskin et al., 2015; Pokhrel et al., 2021; Liu et al., 2021; Zeng et al., 2022; Saide et al., 2022; Shetty et al., 2023). Thus comprehensive and consistent datasets are required to understand and capture these variabilities through

parameterizations of BB aerosol absorption properties. The acquisition of such datasets and the development of improved parameterizations are priorities for BB research.

Second, aerosol absorption properties are still challenging to measure. In recent decades, various measurement approaches have been developed, each with its own advantages and limitations (e.g. Moosmüller et al., 2009; Corr et al., 2009). Probably, the most common in situ technique to measure absorption coefficients of suspended particles is photoacoustic spectroscopy (PAS, e.g., Arnott et al., 1999; Beck et al., 2003; Lack et al., 2012; Sharma et al., 2013; Langridge et al., 2013; Fischer and Smith, 2018). This contactless technique provides real-time data at high temporal resolution. However, accurate PAS measurements require suitable light sources (stable high-power collimated beams) that are challenging to realize for UV wavelengths, particularly below 350 nm. Direct PAS measurements of UV absorption are therefore scarce and have only been applied in laboratory and ground-based settings (Ajtai et al., 2010; Wiegand et al., 2014; Sumlin et al., 2018). In most applications, PAS measurements are limited to a few wavelengths in the visible spectral range. UV absorption properties are inferred via spectral extrapolation, which is associated with large uncertainties (Zeng et al., 2022). In a humid environment (ambient relative humidity $\gtrsim 40\,\%$), additional biases can arise from light-induced particle evaporation (Langridge et al., 2013).

Less direct optical approaches, such as combining cavity enhanced absorption spectroscopy (CEAS) or cavity ringdown spectroscopy (CRDS) for extinction with nephelometry for scattering measurements (e.g., Singh et al., 2016), are also employed. While these methods share most of the limitations inherent to PAS, an additional challenge arises because absorption is calculated as a typically small difference between two large measured quantities (extinction minus scattering). This requires exceptionally high accuracy for both extinction and scattering measurements to yield meaningful absorption results (Massoli et al., 2009).

Absorption properties of soluble BrC compounds are often determined by gathering particles on filters for later analysis. In the laboratory, these particles are extracted from the filters with water or methanol. Insoluble compounds are removed from the solution, and the absorption of the remaining dissolved chromophores is measured using a liquid light waveguide capillary (e.g., Hecobian et al., 2010; Forrister et al., 2015; Liu et al., 2014, 2015a; Zhang et al., 2017). Such measurements can be performed over broad spectral ranges at high resolution. However, reconstructing the absorption of the aerosol in its particulate state requires information on the original morphology and the absorption of insoluble compounds. Usually, information on both these aspects is limited, and uncertainties on reconstructed absorption properties $> 50\,\%$ are not uncommon (Shetty et al., 2019; Zeng et al., 2020, 2022).

Instruments such as the aethalometer or the particle soot absorption photometer (PSAP) calculate particle absorption from transmittance and reflectance of particle-laden filters. Using conveyor-belt filters, such measurements can be performed in a fully automated manner in real-time at sufficient temporal resolution, and over the UV spectral range. However, they are known to suffer from artifacts related to filter-loading and multiple scattering effects (Weingartner et al., 2003; Lack et al., 2008; Cappa et al., 2008; Drinovec et al., 2015).

All of the above measurement techniques are far from ideal, as they alter the original state of the particles, and they have limited sensitivity or suffer from cross-interferences. Various comparison studies show considerable inconsistencies among the different approaches (e.g. Laing et al., 2020; Cheng et al., 2021; Zeng et al., 2022). Clearly, observations and techniques with reliable uncertainty estimates are highly desirable to (1) understand artifacts and inconsistencies in existing methods, (2) identify crucial factors and processes determining the particle absorption, and (3) develop and improve parameterizations of aerosol properties for better prediction of plume radiative transfer in BB scenarios.

The retrieval of aerosol absorption properties from passive spectral observations of solar radiation, offers a valuable complementary approach to in situ measurements. Retrievals have been performed from ground (Petters et al., 2003; Krotkov et al., 2005; Barnard et al., 2008; Corr et al., 2009; Pistone et al., 2019; Jeong et al., 2022), aircraft (Corr et al., 2012) and satellite platforms (Torres et al., 2007; Jethva and Torres, 2011), based on spectral observations of radiance, irradiance and actinic flux (the directionally integrated amount of radiation incident at a given location). Remote sensing provides spectrally continuous sampling of the unaltered aerosol state, down to wavelengths as low as 300 nm. At the same time, remote sensing inherently averages over large parts of the plume, potentially reducing biases from spatial variability. Aerosol optical property retrievals for BB scenarios have, for example, been performed by Corr et al. (2012), showing the potential of this approach. However, Corr et al. (2012) only used wavelengths longer than 350 nm, thus missing the strongest BrC absorptions. Retrievals of aerosol properties from remote sensing observations rely heavily on a priori information of various factors that influence the radiative transfer, such as plume geometry, choice of particle size distribution (PSD), and stratospheric total ozone column. Preferably, these factors are constrained by direct observations or alternatively taken from literature. In both cases they introduce uncertainties that often limit the significance of the retrieval results. Any aerosol optical property retrieval from remote sensing observations thus needs an extensive uncertainty analysis.

In the present study, we have two main goals. First, we aim to assess feasibility and accuracy of UV-Vis remote sensing of aerosol absorption properties in dense BB plumes. Second, we want to compare the determination of absorption properties from aircraft-based comparison measurements and remote sensing observations, and ultimately derive a parame-

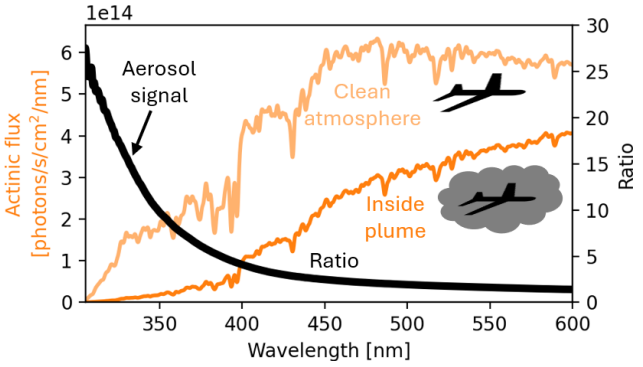


Figure 2. The aerosol absorption signal can clearly be seen in the actinic flux spectra from the CAFS instrument. The ratio of spectra recorded inside and outside of the plume reveals an increasing attenuation towards UV wavelengths.

terization for the aerosol absorption properties. We will use the unique dataset acquired during the FIREX-AQ campaign (Sect. 2), where various young and dense BB plumes were sampled with a comprehensive suite of in situ and remote sensing instruments on the NASA DC-8 research aircraft. The key measurements for our analysis are UV-Vis actinic flux spectra recorded on the aircraft by a Charged-coupled device Actinic Flux Spectroradiometer (CAFS). The sensitivity of these measurements to UV aerosol absorption can easily be demonstrated by comparing two spectra recorded outside and inside the plume, respectively (Fig. 2). Their ratio indicates a strong increase in attenuation towards the UV, whose major portion can unambiguously be attributed to BrC absorption (Tirpitz et al., 2025). This very strong absorption signal allows us to use inverse modeling to derive aerosol absorption properties. In other words, a radiative transfer model is used to simulate actinic flux spectra, and the model results are then fit iteratively to the observed actinic fluxes by varying the aerosol absorption properties in the model.

The FIREX-AQ dataset provides comprehensive and unprecedentedly accurate constraints for remote sensing retrievals and their uncertainties, enabling us to study several fires for a wide range of plume ages. In addition, remote sensing observations were performed for an extended wavelength range down to 298 nm, thus enabling the analysis of the strongest part of the atmospheric BrC absorption. Based on this dataset, we will address the following questions:

1. Can particle UV absorption properties be reliably retrieved from actinic flux spectra in dense BB plumes, considering the various sources of uncertainty?

2. Can we gain new insights regarding biases and inconsistencies in existing measurements?

3. Can we find a parameterization for aerosol UV absorption properties, to better constrain radiative transfer in BB plumes in general?

We introduce a retrieval framework (Sect. 3) based on the VPC (VLIDORT for PhotoChemistry) radiative transfer model (Sect. 3.1). This framework is applied to plume data from three fires sampled during FIREX-AQ (Sect. 2) to retrieve smoke particle imaginary RIs from 308 to 440 nm, and their uncertainties (Sect. 4.1 and 4.2). From the imaginary RI we further derive SSA and volume absorption cross-section (VAC). The latter describes the aerosol absorption cross-section per aerosol volume in units of μm^{-1} (Bond and Bergstrom, 2006). The more common mass absorption cross-section (MAC) can be obtained by dividing by an appropriate particle material density.

We compare our results to aircraft-based filter sampling and in situ photoacoustic measurements from FIREX-AQ to assess method agreement and reliability (Sect. 4.3), and propose new parameterizations for the dependence of imaginary RI, VAC and SSA on wavelength and plume age (Sect. 4.6).

2 FIREX-AQ campaign

The present study is based on data from the NOAA/NASA Fire Influence on Regional to Global Environments and Air Quality (FIREX-AQ) measurement campaign (Warneke et al., 2023). This 6-week campaign took place in the Western US from July to September 2019, and comprised sampling of more than 90 wildfire plumes with a variety of in situ and remote sensing instrumentation on the NASA DC-8 research aircraft. The full dataset is available at https://www-air.larc.nasa.gov/missions/firex-aq/ (last access: 10 October 2026) (Aknan and Chen, 2023).

2.1 Investigated fires

In the present study, we performed retrievals for three fires: Shady, Lefthand, and Williams Flats. These fires evolved under clear-sky ambient conditions; this consideration simplifies the radiative transfer modeling. Table 1 provides an overview of the fire occurrences and their key characteristics, such as plume aerosol optical depth (AOD), burned fuel, and meteorological conditions.

Figure 3 shows a typical flight path through the Shady fire. The aircraft crossed the plume in transects perpendicular to the wind direction, and in sequentially increasing distances (steps of $\approx$ 10 km) to the fire. At a distance of about 100 km from the fire, the aircraft returned to the original starting point, repeating the transect pattern over the plume.

2.2 Key instruments

The key FIREX-AQ observations for the present study are the actinic flux spectra from which aerosol absorption properties are retrieved. However, ancillary FIREX-AQ measurements were used to constrain other relevant environmental parameters; these include atmospheric conditions, particle

Table 1. Investigated fires

Name	Shady	Lefthand	Williams flats
Date	25 July	30 July	3 August
Latitude	44.517	46.933	47.939
Longitude	−115.019	−120.9930	−118.618
State	ID	WA	WA
Fuel	Timber, tall grass	Timber, logging slash	Dead trees, grass, sage bitter brush
Max. AOD[a]	9.8	0.5	11.3
SZA [°][b]	47–82	73–79	43–78
Smoke age [hh:mm]	00:15–03:10	04:50–06:30	00:30–06:50
MCE[c]	0.88 ± 0.02	NA[d]	0.92 ± 0.02
Wind [ms^{-1}]	8.9 ± 3.3	7.4 ± 1.6	4.1 ± 1.3
Wind dir. [°][e]	270 ± 18	265 ± 8	270 ± 30
Humidity [%]	33 ± 5	35 ± 1	20 ± 13
Transects	20	5	22
Lidar profiles[f]	284	39	564

[a] At 400 nm. [b] Retrievals ultimately limited to SZA ≤ 75° (Sect. 4.1). [c] Mass combustion efficiency (Stockwell et al., 2014). [d] CO enhancement too low for reliable MCE calculation. [e] Clockwise with respect to North. [f] Complete profiles with plume AOD > 0.2.

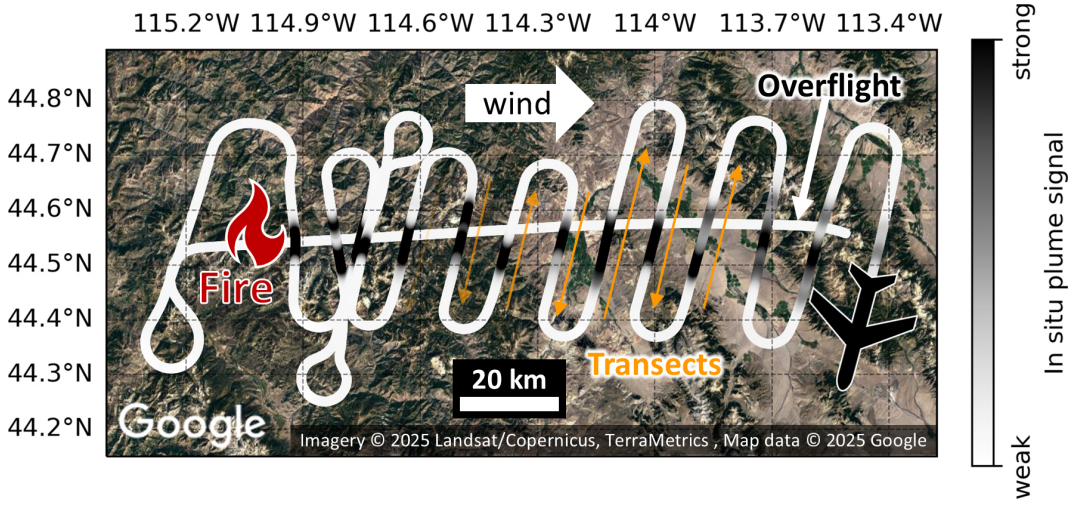


Figure 3. A segment of the flight path sampling the Shady fire plume, illustrating the typical flight pattern. The aircraft crossed the plume in so-called "transects" perpendicular to the wind direction, and in sequentially increasing distances (steps of ≈ 10 km) to the fire. Track color indicates plume signal based on in situ carbon monoxide measurements.

size and plume geometry. The following paragraphs introduce the most relevant instruments. Assimilation of the data into the retrieval is described in Sect. 3.

Actinic flux spectra were recorded by the CAFS instrument onboard the NASA-DC8 aircraft (Shetter and Müller, 1999; Hall et al., 2018). This instrument combines data from two channels with upward and downward-facing entrance optics, to capture radiation over the full 4π steradian solid angle. The instrument was calibrated in the laboratory to provide absolute actinic flux density spectra in units of photons s^{-1} cm^{-2} nm^{-1}. It covers the spectral range from 298 to 640 nm at a resolution of 1.7 nm (FWHM) at 297 nm and ≈ 0.8 nm sampling. Typical spectra are shown in Fig. 2. Its limit of detection is 6×10^{10} photons s^{-1} cm^{-2} nm^{-1}, a value determined from noise analysis under low light conditions. The error in sensitivity was estimated to be 5 % and arises from uncertainties in the instrument's calibration.

The aerosol spatial distribution was constrained using Lidar observations from the aircraft, from an instrument called DIAL-HSRL, which combines a High Spectral Resolution Lidar (HSRL, Hair et al., 2008) and an ozone DIfferential Absorption Lidar (DIAL, Browell, 1989). The Lidar observations were complemented by in situ measurements of the aerosol extinction, absorption, and scattering coefficients, using TSI Nephelometers, a Radiance Research Particle Soot Absorption Photometer (PSAP), and the NOAA Aerosol Op-

tical Properties Suite (AOP, Langridge et al., 2011; Lack et al., 2012). The data were combined and processed as described in Tirpitz et al. (2025) to infer vertical profiles of the aerosol extinction coefficient at 532 nm, at a temporal resolution of 10 s (equivalent to a horizontal spatial resolution of 1.5 km at the average speed of the aircraft of about $150\,\mathrm{ms}^{-1}$) and a vertical resolution of 30 m (Fig. 5). Time series of these profiles (Lidar curtains) for the individual transects are shown in panel A of Fig. 5, and in Figs. S3 and S4 in the Supplement.

A TSI model 3340 laser aerosol spectrometer measured aerosol size distributions at 1 s temporal resolution, at aircraft cabin temperature and dry humidity. Hygroscopic growth effects were neglected, since relative humidities during the investigated flights were $< 40\,\%$ (Table 1). Under these conditions, scattering enhancements for BB aerosol are reported to be $\lesssim 1\,\%$ (Kotchenruther and Hobbs, 1998; Chang et al., 2023).

For the physical plume age, i.e. the residence time of the smoke in the atmosphere since emission, we use data from the FIREX-AQ database (Aknan and Chen, 2023). These are the "wind uncorrected" plume ages, calculated as described in Holmes et al. (2025) by backtracking upwind trajectories from the aircraft to the source fire location using the NOAA HYSPLIT model (Stein et al., 2015).

The DC-8 aircraft meteorology and navigation systems provided temperature, pressure, humidity, wind speed, wind direction, geolocation, altitude above sea level, ground speed, and radar measured altitude above ground at 1 s temporal resolution.

3 Retrieval setup

We developed a general retrieval scheme that can be applied at any given time in the flight. The basic idea is (1) to use a radiative transfer model with the capability to model actinic flux spectra, (2) constrain the model with information from ancillary FIREX-AQ measurements and literature data, and (3) to vary the a priori aerosol absorption properties in the model in order to match the coincident CAFS actinic flux measurement. To obtain reliable estimates of the retrieval uncertainties for a wide range of measurement conditions, the framework includes an error propagation scheme, considering uncertainties from the CAFS measurements, ancillary constraints, and simplifying assumptions in the modeling approach. Fig. 4 provides a schematic overview of the framework. Details of each element are discussed in the following subsections. Key quantities in this scheme and their mathematical expressions (we follow the notation by Rodgers, 2000) used throughout this paper are the following:

1. The measurements, summarized in the vector $\boldsymbol{y}$: They comprise the CAFS measurements of up- and downwelling actinic fluxes at various wavelengths λ (Sect. 3.4).
2. The critical fixed model input parameters, summarized in the vector $\boldsymbol{b}$. These are model inputs that will not be varied during the fit, but are critical to constrain atmospheric state and radiative transfer. They are inferred from FIREX-AQ aircraft measurements or satellite observations, or taken from literature (Sect. 3.5).
3. The fit parameters, which are elements of the vector $\boldsymbol{x}$, describe the aerosol absorptive properties and will be varied in order to bring model simulations and measurements into agreement. The fit result is denoted as $\hat{\boldsymbol{x}}$.
4. The radiative transfer model, in the following equations referred to as the vector function $\boldsymbol{F}(\boldsymbol{x}, \boldsymbol{b})$.

To find the solution $\hat{\boldsymbol{x}}$, we use the "optimize.least_squares" method from the SciPy Python library (Virtanen et al., 2020). This method minimizes a weighted least-squares cost function

$$\chi^2 = (\boldsymbol{F}(\boldsymbol{x}, \boldsymbol{b}) - \boldsymbol{y})^T \, \mathbf{C}_\mathrm{y}^{-1} \, (\boldsymbol{F}(\boldsymbol{x}, \boldsymbol{b}) - \boldsymbol{y}) \tag{1}$$

applying a Levenberg-Marquardt iteration scheme (Levenberg, 1944; Marquardt, 1963), where $\mathbf{C}_\mathrm{y}$ is the measurement error covariance matrix (Sect. 3.6).

3.1 Radiative transfer model **F**

We use the 1D radiative transfer model VPC (VLIDORT for PhotoChemistry, Tirpitz et al., 2025), built around the Quasi-Spherical Vector Linearized Discrete Ordinate Radiative Transfer (VLIDORT-QS) code (Spurr et al., 2022). The model simulates actinic fluxes for a given atmospheric state, solar geometry, and observer altitude. The atmospheric state is described in terms of various model input parameters, including aerosol properties and aerosol vertical profile (details in Sect. 3.5 and 3.3). For plumes that are several kilometers wide and for solar zenith angles $\lesssim 75°$, Tirpitz et al. (2025) showed that the application of 1D radiative transfer models such as VPC, is highly successful: Comparisons between modeled and measured actinic fluxes showed that 3D radiative effects can occasionally be significant for individual data points (10 s temporal resolution) in areas with large extinction gradients, such as plume edges. However, transect-averaged measurements agreed very well with the model, confirming minimal 3D effects in this approach.

3.2 Representation of plume aerosol

In the model, we approximate plume particles as an ensemble of homogeneous spherical particles of uniform composition. For their representation we make use of VPC's "microphysical aerosol" module (Tirpitz et al., 2025), which characterizes the ensembles in terms of a bimodal log-normal PSD, the complex refractive index $n(\lambda) + ik(\lambda)$ of the particle material and a vertical extinction coefficient profile $E(\lambda_0)$ at a predefined reference wavelength λ_0. This simplified aerosol

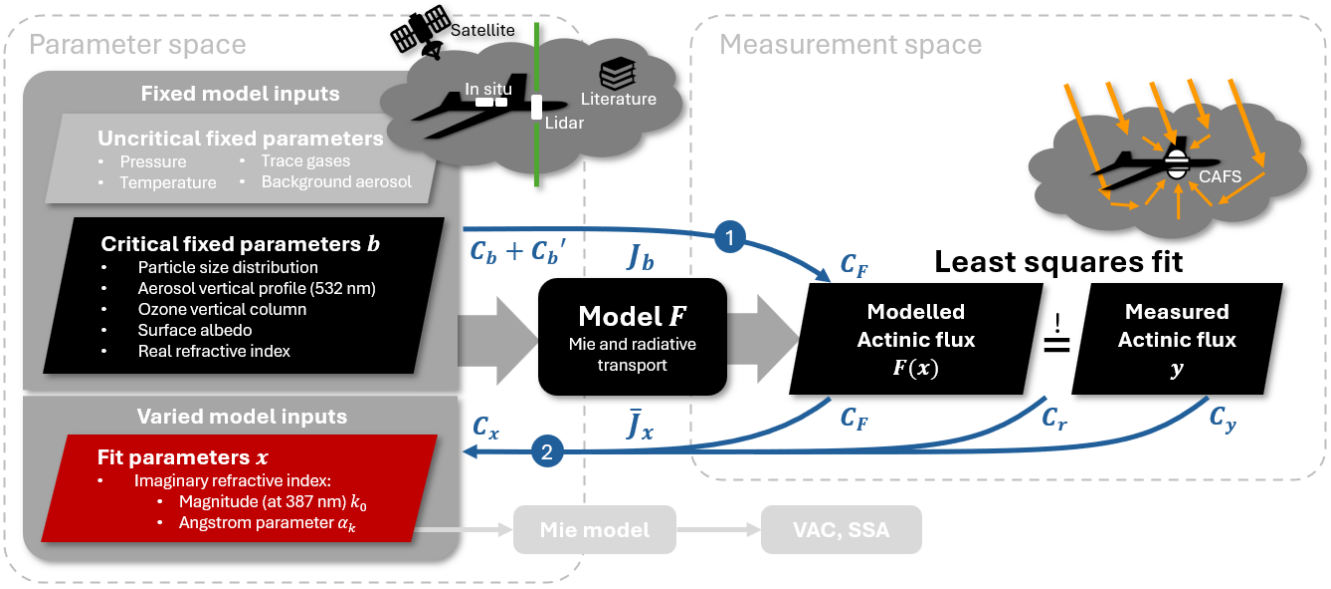


Figure 4. Schematic diagram of the retrieval setup. The left side provides an overview of the various model inputs. Most relevant are the fixed critical parameters (Sect. 3.5) and the fit parameters (Sect. 3.3), mathematically represented by the vectors $\boldsymbol{b}$ and $\boldsymbol{x}$ in the parameter vector space. Both critical and uncritical fixed parameters are constrained by external data from aircraft, satellite or literature. The retrieval is performed by minimizing the least-squares residual between model results and measurements, represented by the vectors $\boldsymbol{F}(\boldsymbol{x})$ and $\boldsymbol{y}$ in the measurement vector space. Once the imaginary RI has been successfully retrieved, further parameters like VAC, MAC and SSA are derived using a Mie code. Blue arrows and symbols illustrate the error propagation strategy (Sect. 3.6). Symbols $\mathbf{C}$ indicate covariance matrices, symbols $\mathbf{J}$ indicate Jacobian matrices.

representation was chosen to (1) best accommodate available FIREX-AQ measurements, (2) minimize the number of retrieved parameters, given the limited information in the spectra, and (3) align with the Mie aerosol representation commonly used for radiative transfer calculations in current chemical transport and climate models (Bond and Bergstrom, 2006; Stevens and Dastoor, 2019). The description is complete in the sense that all bulk optical properties (extinction coefficient, SSA and scattering phase function) can be calculated for arbitrary wavelengths and altitudes by running VPC's integrated Mie model. The imaginary RI is the parameter of primary interest in this study and the target quantity of the retrieval (Sect. 3.3).

It should be noted that the retrieved imaginary RI represents a "Mie equivalent" value. RI values for actual particles may differ due to specific mixing state and particle morphology. At the same time, this Mie-equivalent RI value is "radiatively correct" in the sense that the Mie code will yield optical bulk properties (extinction cross-section, SSA, scattering phase function) that are close to reality. Furthermore, the homogeneous sphere representation underlying the Mie-equivalent approach is often used in satellite retrievals and chemical transport models. This makes our results directly transferrable.

Nevertheless, we performed sensitivity studies for more complex particle representations, to estimate direction and approximate magnitude for the biases induced by our homogeneous sphere assumption. For particles with a core-shell morphology (core is BC, shell is BrC, BrC / BC volume ratio and PSD same as in the homogeneous case), our retrieval overestimates the particle average imaginary RI by $\approx 10\,\%$ and underestimates its Angstrom coefficient by ≈ 0.15. For particles that are externally mixed (pure BC particles, pure BrC particles), our retrieval underestimates the particle average imaginary RI by $\approx 10\,\%$ and overestimates its Angstrom coefficient by 0.3. These numbers are within the uncertainties of our retrieval. Furthermore, we investigated potential impacts of ammonium nitrate (NH_4NO_3) coating on the aerosol optical properties, as reported, e.g., by Yuan et al. (2020). High-resolution Aerosol Mass Spectrometer measurements (see FIREX-AQ database, Aknan and Chen, 2023) during the three analyzed flights imply NH_4NO_3 volume fractions of 1.9 %–2.4 %. Assigning all particulate nitrate to NH_4NO_3 gives conservative upper bounds of 2.4 %–3.3 %, with a transect-averaged maximum of 7 %. Core-shell Mie calculations using 2.5 %, 3.5 %, and 7 % volume fractions of non-absorbing NH_4NO_3 shells ($n = 1.55$) changed absorption by at most 6 % and single-scattering albedo by equal to or less than 0.01. As illustrated in Sect. S2, these changes are about an order of magnitude smaller than the changes introduced by the size uncertainties assumed in our error propagation scheme (see Sect. 3.6) and thus have no significant impact on the retrieval results.

3.3 Retrieved model input parameters $\boldsymbol{x}$

The goal of the retrieval is to infer the wavelength dependent imaginary refractive index $k(\lambda)$ of the aerosol material. To reduce the number of retrieved parameters, we do not retrieve independent values $k(\lambda)$ at multiple wavelengths. Instead, we assume an Angstrom wavelength dependence

$$k(\lambda) = k(\lambda_0)\left(\frac{\lambda_0}{\lambda}\right)^{\alpha_k} \quad (2)$$

and we then retrieve the Angstrom coefficient α_k, plus magnitude $k(\lambda_0)$ at a reference wavelength of $\lambda_0 = 387\,\text{nm}$. These two parameters constitute the parameter vector $\boldsymbol{x} = (k(\lambda_0), \alpha_k)$. Adding higher order terms to Eq. 2 had only a small impact and was thus not implemented.

The retrieved state vector elements combined with information on the size distribution and real RI (see Sect. 3.5), enable calculations of the imaginary refractive index, and the SSA and VAC at other wavelengths.

3.4 Measurements $\boldsymbol{y}$

The measurement vector $\boldsymbol{y}$ in our retrieval scheme contains $m = 18$ values: these are the logarithm of CAFS upwelling and downwelling actinic fluxes, each at 9 selected wavelengths (308, 313, 322, 332, 347, 364, 387, 405, 440 nm). Instead of the full spectra provided by the CAFS, this reduced set of wavelengths has been selected to improve computational efficiency, while still capturing the spectrally smooth aerosol signal. The wavelengths are specially chosen to avoid interference with strong solar Fraunhofer lines. To temporally match the CAFS and the Lidar, the 1 Hz CAFS data was averaged over the 10 s Lidar measurement window. The logarithmic transformation of $\boldsymbol{y}$ improves model linearity, numerical stability, and representativeness of uncertainties, considering the exponential nature of the Beer-Lambert law.

3.5 Fixed model inputs $\boldsymbol{b}$

The fixed model inputs were constrained with ancillary FIREX-AQ aircraft measurements, satellite observations and literature data. We distinguish between uncritical and critical fixed inputs, based on their relevance to the modeled actinic fluxes and ultimately to the retrieval results.

Uncritical fixed parameters have a negligible impact on the modeled actinic flux ($< 3\,\%$ when uncritical input is varied within its uncertainty) and are not considered in the retrieval error propagation scheme (Sect. 3.6). They comprise the pressure profile, temperature profile, NO_2 profile and background aerosols, and are constrained following the procedures described in detail in Tirpitz et al. (2025). Table 2 provides an overview of all uncritical fixed inputs, along with short descriptions of the respective sources of information (FIREX-AQ instrument or literature reference).

Critical fixed parameters have a higher impact on modeled actinic flux and are considered in the retrieval error propagation scheme (Sect. 3.6). Critical fixed inputs are the PSD, the aerosol vertical profile, the ozone vertical profile, the surface albedo and the real part of the plume aerosol RI. Except for the real RI, the critical fixed inputs are constrained following the procedures in Tirpitz et al. (2025), a summary of which is provided in the following paragraphs.

PSDs were measured in situ by a laser aerosol spectrometer on the aircraft. For the retrieval we use transect-averaged data, to reduce measurement noise, while still capturing changes in particle size with plume age (Sect. S1). The Mie module of VPC describes particle sizes in terms of a normalized multi-modal log-normal size distribution, described via median radii, modal widths, and modal fraction for each mode. These model input parameters were inferred by fitting a bimodal distribution to the observed PSDs. The bimodal distribution describes the observed PSDs accurately (see Sect. S2). The amount and spatial distribution of aerosols are described through vertical profiles of the aerosol extinction coefficient at 532 nm. These are inferred combining Lidar observations and in situ measurements, both performed on the aircraft (Sect. 2.2). Conversion to the actual retrieval wavelengths in the UV-Vis (Sect. 3.4) is performed on-the-fly at each inverse-model iteration, based on derived aerosol microphysical properties from the current iteration. The surface albedo is constrained using the TROPOMI database for monthly Lambertian-equivalent reflectivity (LER, Tilstra et al., 2024), which is integrated into the VPC model. The O_3 tropospheric profile is inferred from O_3 in situ measurements during ascent and descent of the corresponding flight. For the stratospheric profile we assumed the 1976 US Standard Atmosphere, scaled according to OMI satellite observations (Bhartia, 2012).

The most critical fixed parameter in our retrieval is the real RI $n(\lambda)$ of the aerosol. During FIREX-AQ, no direct measurements of $n(\lambda)$ were performed. Based on literature review and FIREX-AQ related investigations presented in Saide et al. (2022), we choose a fixed value of $n = 1.52$ for all wavelengths.

3.6 Error propagation scheme

Finding a realistic uncertainty estimate for the retrieval results $\hat{\boldsymbol{x}}$, based on the various uncertainties and assumptions involved in the retrieval, constitutes a major challenge. Sources of uncertainty are present in both the parameter space (e.g. errors in the critical fixed parameters) and the measurement space (e.g. CAFS measurement error). Combining these requires propagation of error contributions through the radiative transfer model $\boldsymbol{F}$ in both the forward direction (from the parameter to the measurement space) and the backward direction (from the measurement to the parameter space). For this purpose, we resort to the most general approach for linear propagation of statistical errors: the for-

Table 2. Overview of the uncritical fixed model parameters and how they are constrained during the retrieval. A more detailed explanation of the retrieval process can be found in Tirpitz et al. (2025).

	Parameter	Data source description
Tropospheric background aerosol	Size distribution	Laser aerosol spectrometer measurements outside plume
	Refractive index	Literature (Levoni et al., 1997)
	Extinction profile	Lidar extinction profiles outside plume
Stratospheric background aerosol	Size distribution	Literature (Wrana et al., 2021)
	Refractive index	Literature (Levoni et al., 1997)
	Extinction profile	SAGE II database (SAGE Science Team, 2012)
Other	Pressure profile	Std. atmosphere, scaled with in situ
	Temperature profile	Std. atmosphere, troposphere scaled with in situ
	NO_2 profile	Lidar aerosol profile scaled by in situ NO_2 : aerosol-ratio

malism for error propagation with covariance matrices (e.g. Strutz, 2011; Tellinghuisen, 2001; Rodgers, 2000). This approach is based on the equation

$$\mathbf{C}_\mathrm{f} = \mathbf{J}\,\mathbf{C}_\beta\,\mathbf{J}^\mathrm{T} \tag{3}$$

where $\mathbf{C}_\mathrm{f}$ is the covariance of some function or model $\boldsymbol{f}(\boldsymbol{\beta})$, resulting from covariances $\mathbf{C}_\beta$ in the input parameters $\boldsymbol{\beta}$, propagated using the Jacobian matrix

$$\mathbf{J} = \frac{\partial \boldsymbol{f}}{\partial \boldsymbol{\beta}} \tag{4}$$

Here, the "T" suffix denotes matrix transpose.

This formalism is applicable to any vector-valued function and considers potential correlations between errors, represented by the off-diagonal elements of the covariance matrices. It should be noted that for a multivariable scalar function $f(\boldsymbol{\beta})$ and uncorrelated errors, Eq. 3 reduces to the much more familiar equation for error propagation:

$$\Delta f^2 = \sum_i \left(\frac{\partial f}{\partial \beta_i}\right)^2 \Delta\beta_i^2 \tag{5}$$

For our retrieval, we consider the following error contributions: (1) uncertainties in the CAFS measurements, (2) uncertainties in the fixed model parameters, (3) errors arising from model simplifications, and (4) the fit residual to capture potential failures in convergence of the fit. For these initial uncertainties, we construct covariance matrices, assuming the errors to be uncorrelated, i.e. the off-diagonal elements of these covariance matrices are identically zero. The measurement covariance matrix $\mathbf{C}_\mathrm{y}$ is constructed based on the CAFS measurement uncertainties $\Delta\boldsymbol{y}$ (see Sect. 2.2). The covariance of the fixed model parameter $\mathbf{C}_\mathbf{b}$ is constructed similarly, assuming the uncertainties $\Delta\boldsymbol{b}$ listed in Table 3. Uncertainties arising from model simplifications are considered by additional uncertainties in distinct model input parameters, which lead to similar errors in the modeling results as one would expect from the actual model simplifications. These errors, $\Delta\boldsymbol{b}'$, are listed in Table 3 and are represented by the covariance matrix $\mathbf{C}'_\mathbf{b}$. They are applied to (1) the PSD radii to account for the simplified representation of aerosols as homogeneous and spherical particles, (2) the aerosol optical depth to account for horizontal inhomogeneity of the plume and related 3D radiative transfer effects, and (3) the surface albedo to account for horizontal inhomogeneity in surface properties. The fit residual is represented by the covariance matrix $\mathbf{C}_\mathrm{r}$, with the squared residual elements $(F_i(\hat{\boldsymbol{x}}) - y_i)^2$ on the diagonal. It captures the cases in which the simplified model cannot reproduce the real observations, most noteworthy in scenarios where the assumption of a simple angstrom dependence of k does not hold.

The complete error propagation scheme is qualitatively illustrated by the blue arrows and symbols in Fig. 4. The scheme unfolds in two major steps, indicated by the upper and lower light-blue arrows, respectively. In the first step, we forward propagate $\mathbf{C}_\mathbf{b}$ and $\mathbf{C}'_\mathbf{b}$ through the model to obtain a "model covariance" $\mathbf{C}_\mathrm{F}$ in the measurement space. This covariance describes the uncertainties in the modeled actinic fluxes that arise from uncertainties in the critical fixed model inputs and model simplifications. In accordance with equation 3, it is calculated as

$$\mathbf{C}_\mathrm{F} = \mathbf{J}_\mathbf{b}\,(\mathbf{C}_\mathbf{b} + \mathbf{C}'_\mathbf{b})\,\mathbf{J}_\mathbf{b}{}^\mathrm{T} \tag{6}$$

using the radiative transfer model Jacobians with respect to the fixed input parameters:

$$\mathbf{J}_\mathbf{b} = \frac{\partial \boldsymbol{F}(\boldsymbol{x}, \boldsymbol{b})}{\partial \boldsymbol{b}}. \tag{7}$$

In the second step, the covariances in the measurement space ($\mathbf{C}_\mathrm{F}$, $\mathbf{C}_\mathrm{r}$ and $\mathbf{C}_\mathrm{y}$) are combined and propagated back through the model to obtain the fit result covariance

$$\hat{\mathbf{C}}_\mathbf{x} = \bar{\mathbf{J}}_\mathbf{x}\,(\mathbf{C}_\mathrm{F} + \mathbf{C}_\mathrm{r} + \mathbf{C}_\mathrm{y})\,\bar{\mathbf{J}}_\mathbf{x}{}^\mathrm{T}, \tag{8}$$

using the weighted Moore-Penrose inverse (also referred to as weighted generalized inverse or gain matrix in literature):

$$\bar{\mathbf{J}}_\mathbf{x} = (\mathbf{J}_\mathbf{x}{}^\mathrm{T}\mathbf{C}_\mathrm{y}^{-1}\mathbf{J}_\mathbf{x})^{-1}\mathbf{J}_\mathbf{x}{}^\mathrm{T}\mathbf{C}_\mathrm{y}^{-1}. \tag{9}$$

Table 3. Assumed uncertainties for the fixed model inputs

Parameter b_i	Δb_i	$\Delta b_i'$
PSD radii	10 %	20 %
Real refractive index	0.1	
Aerosol extinction profile	15 %	20 %
Ozone vertical column	5 %	
Surface albedo	30 %	40 %

Here, $\mathbf{J_x}$ are the Jacobians with respect to the retrieved parameters

$$\mathbf{J_x} = \frac{\partial \boldsymbol{F}(\boldsymbol{x}, \boldsymbol{b})}{\partial \boldsymbol{x}}. \tag{10}$$

With the retrieval state vector having just two elements, $\hat{\mathbf{C}}_\mathbf{x}$ is a 2×2 matrix providing the uncertainties for the retrieved imaginary RI and its Angstrom coefficient

$$\Delta\hat{k}(\lambda_0) = \sqrt{\hat{C}_{x,11}} \quad \text{and} \quad \Delta\hat{\alpha}_k = \sqrt{\hat{C}_{x,22}}. \tag{11}$$

as well as their correlation coefficient

$$\hat{r} = \frac{\hat{C}_{x,12}}{\sqrt{\hat{C}_{x,11}\hat{C}_{x,22}}}. \tag{12}$$

4 Retrieval application and post-processing

Our goal is to determine the average aerosol absorption properties on a transect basis, as they will form the dataset for our analysis. Calculation of these transect averages is performed in multiple steps as outlined in the following subsections.

4.1 Retrievals on individual profiles

In a first step, we apply the retrieval scheme described in Sect. 3 to each Lidar profile where (1) vertical gaps in the Lidar profile are absent or can reliably be interpolated and (2) the AOD is > 0.2. This results in 10–20 individual retrievals per plume transect at 10 s temporal resolution. For all three fires, we perform nearly 900 retrievals (see Table 1). As these retrievals include any data with a notable plume signal, they cover a broad range of conditions. We use this set of results to assess (1) the ideal conditions for accurate and stable retrievals, (2) the reliability of propagated errors, and (3) the contribution from various error sources to the total uncertainty in the retrieval results.

Figure 5 shows a time series of the lidar profiles and the imaginary RI retrieval results in terms of k_0 (at $\lambda_0 = 387$ nm) and α_k for the Shady fire. Section S3 provides similar plots for the Lefthand and Williams Flats fire.

At first glance, the retrieval results show significant variability within and between transects (Fig. 5B and C). However, there are clear indications that the quality of the retrieval strongly depends on the geometrical configuration and the underlying atmospheric conditions and that particularly large variations originate from retrieval artifacts rather than from any real variations of the plume aerosol properties.

Based on our sensitivity studies in Sect. S4 and Tirpitz et al. (2025) and considering the limitations of the 1D radiative transfer model, most reliable results are expected when the aircraft is inside the plume, the AOD is moderate, the horizontal variability is low, and the sun is relatively high in the sky (SZA $< 75°$). For retrievals where these conditions are met, the variability in the retrieval results is relatively small and the propagated errors in $k(\lambda_0)$ and α_k are on the order of 20 % and 15 %, respectively. A few examples of such retrievals are highlighted by the green shading in panels B and C of Fig. 5. For the imaginary RI $k(\lambda)$, this translates into uncertainties of about 20 % in the UV and 25 % in the visible (example shown in Fig. S7, top row). In these cases, the errors are dominated by uncertainties in the critical fixed parameters $\mathbf{C}_\mathrm{F}$ (Fig. 5E), with the highest contributions from the real RI of the aerosol and the plume AOD (green and blue areas in Fig. 5F). Interestingly, the sensitivity to the PSD (red, Fig. 5F) is relatively small, i.e., similar retrievals for other plumes are conceivable in the future, even in scenarios where the PSD is not as well constrained as was the case during FIREX-AQ.

On the other hand, there are scenarios where conditions are less favorable. For example, for low AODs, the aerosol signal in the spectra is small, rendering the retrieval susceptible to inaccurate assumptions about surface properties, the presence of thin clouds, or horizontal inhomogeneities. Furthermore, when the aircraft is far above, well below, or close to the edge of the plume, 3D radiative transfer effects not captured by the model, such as shadowing and side-illumination, become increasingly probable. As a result, the retrieval occasionally becomes unstable and yields extreme or even unrealistic values for k_0 and α_k. Such scenarios are sometimes captured by the error propagation scheme, in terms of correspondingly large associated uncertainties (example indicated by the orange shading in Fig. 5), which provides confidence in our error propagation scheme to reflect the quality of the conditions and results well. However, accounting accurately for all detrimental effects is impractical and, for extreme scenarios, the non-linearity of the problem can cause the error propagation scheme to fail (example indicated by the red shading in Fig. 5). Consequently, it becomes necessary to apply additional filters, as described in detail in Sect. 4.2.

The error magnitudes shown in Fig. 5E indicate that the contribution of the fit residual $\mathbf{C}_\mathrm{r}$ to the propagated retrieval error typically stays below the contribution of the model error $\mathbf{C}_\mathrm{F}$, indicating a successful convergence of the fit within the limits of the model. During in-plume observations at high SZAs, the retrieval error is dominated by the increasing measurement noise $\mathbf{C}_\mathrm{y}$ of the CAFS measurements (Fig. 5E, transects 17–20) due to low-light conditions.

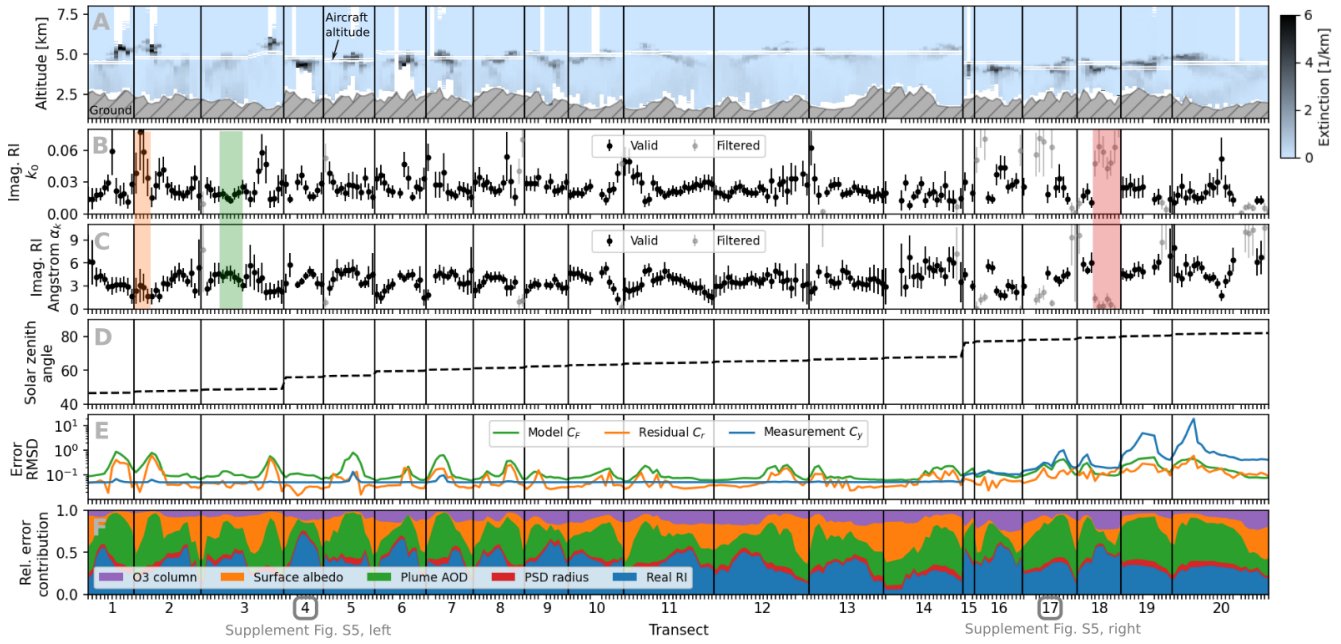


Figure 5. Results from retrievals performed on individual lidar profiles from the 20 transects crossing the Shady fire. Similar timeseries for the Williams Flats and Left hand fires can be found in Sect. S3. Panel **(A)** shows the plume cross-sections in terms of Lidar curtains of aerosol extinction coefficient. Panels **(B)** and **(C)** show the retrieval results in terms of imaginary RI magnitude k_0 (at 387 nm) and the Angstrom coefficient α_k. Error bars indicate propagated uncertainties according to Eq. 11. Grey data points are flagged as invalid according to the filter criteria described in Sect. 4.2. Panel **(D)** shows solar zenith angle. Panel **(E)** indicates contributions from the model error $\mathbf{C}_\mathrm{F}$, fit residual $\mathbf{C}_\mathrm{r}$ and measurement error $\mathbf{C}_\mathrm{y}$ to the total retrieval uncertainty $\hat{\mathbf{C}}_\mathbf{x}$. Values represent root-mean-square differences (RMSDs) over the diagonal of the corresponding covariance matrix. Panel F illustrates the relative contributions of each critical fixed parameter to the total model covariance $\mathbf{C}_\mathrm{F}$. As indicated on the transect x-axis, results for transects 4 and 17 are shown in more detail in Sect. S7.

4.2 Calculation of transect averages

To obtain the final absorptivity results discussed in the result sections, we calculate average values for each transect from the time series in Fig. 5. The averaging smoothes out small-scale variability and retrieval instabilities, thereby providing more reliable results, while major dependencies, e.g., on the plume age, can still be investigated.

To reduce biases introduced by extreme outliers, we apply additional filtering, as noted above in Sect. 4.1. We generally find that unrealistic retrieval results occur when we obtain very large values in k_0 and very low values in α_k, or vice versa. We therefore apply a filter based on the k_0/α_k ratio. We discard retrieval results where k_0/α_k deviates from the k_0/α_k median by more than a factor of 5 or 0.2 in the upper or lower direction, respectively. In our dataset for all three fires, this filtering removes 14 % of the retrievals. Allowing for larger or smaller deviations in k_0/α_k affects the variability of our results, but does not introduce significant biases in the transect-averaged values (Fig. S9). During transect averaging of the filtered data, individual retrievals are weighted by their propagated error, such that the averages are driven by the most reliable retrievals. We use the weighted average of the propagated errors of the individual retrievals to represent the uncertainties of the transect averages. This is a conservative approach, but quite reasonable, considering that many of the contributing errors are expected to systematically bias individual retrievals in a common direction (such as biases arising from the fixed real RI, PSD size calibration, Lidar ratio estimates for the current transect, etc.).

In the Supplement (Fig. S7) we present examples showing how the averaging process successfully calculates transect-averaged spectrally resolved RI, VAC, and SSA for a case where retrievals vary little during a transect and one where larger systematic variations are encountered.

Based on the approach described in Sect. 4, we derive transect-averaged imaginary RI and Angstrom exponents for all three investigated fires (Fig. 6A). The retrieved imaginary RIs vary between 0.02 and 0.03 between transects with uncertainties below 0.01. The Angstrom exponents vary between 3 and 5, with uncertainties below 1. Outliers in k_0 and α_k, as for instance occurring for transects 5 and 6 during the Lefthand fire (Fig. 6A), can be attributed to non-ideal conditions such as low AOD, which are partly captured by the error propagation scheme and associated with correspondingly large uncertainties in α_k.

To further illustrate our results, we calculate VACs and SSAs at three wavelengths (Fig. 6B and C). We observe the expected strong increase in absorption towards shorter

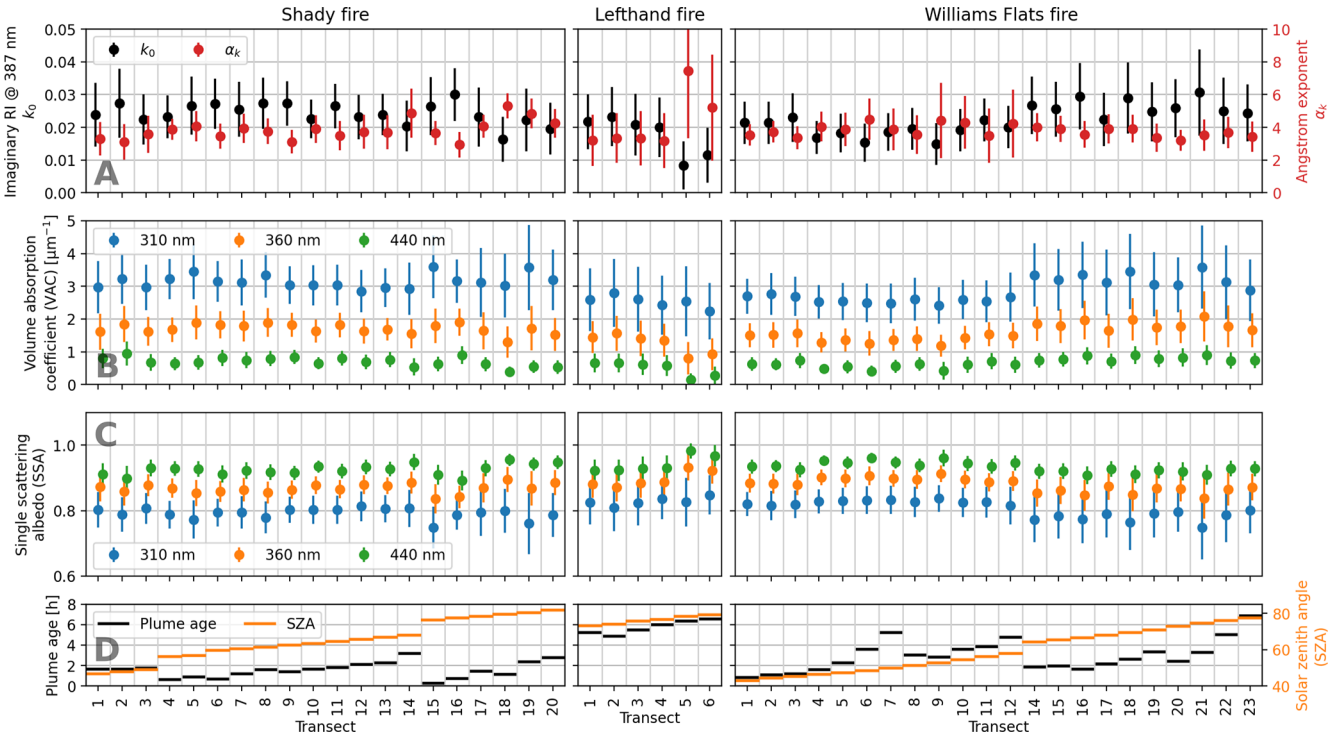


Figure 6. The final transect-averaged retrieval results for all three investigated fires. Panel **(A)** shows the directly retrieved parameters (imaginary RI k_0 at 387 nm and Angstrom exponent α_k). Panels **(B)** and **(C)** show derived VACs (SSAs) at three wavelengths. Panel **(D)** shows physical plume age and solar zenith angle.

wavelengths. Although the different transects comprise varying numbers of individual retrievals and variability among them (e.g. Fig. S7A and C), the transect averages are mostly consistent, within the uncertainty estimates (Fig. 6). Surprisingly, the values are similar between the three different fires, in particular towards shorter wavelengths (Fig. 6B and C). The dependence of the optical properties on plume age (the latter is shown in Fig. 6D), will be analyzed in more detail in Sect. 4.4.

Transect-averaged imaginary RI and Angstrom exponents, as well as VAC and SSA derived from them, are in line with previous studies (as, for example, reviewed in Laskin et al. (2015)) and coincident aircraft-based comparison measurements, which we will discuss further in Sect. 4.3.

4.3 Comparison with coincident aircraft-based measurements

During the Shady fire flight, our retrievals coincided with two independent aircraft-based UV-visible aerosol absorption datasets: filter samples analyzed offline by spectral analysis of extracted BrC chromophores (SAEB), and real-time in situ measurements by photoacoustic spectroscopy (PAS). These datasets provide complementary points of comparison with our remote sensing results.

The first comparison dataset, referred in the sequel to as SAEB (spectral analysis of extracted BrC chromophores), is based on aircraft filter collection followed by offline solvent extraction and spectrophotometric analysis, and is therefore not strictly an in situ measurement in the same sense as PAS. Particles were collected on separate filters for each transect. The filters were then extracted with water and afterwards with methanol. While most organic material dissolves in either of these solvents, insoluble black carbon remainders can be removed from the solution using pore filters. The absorption coefficients of the solutions between 300 and 700 nm were determined using a Liquid Waveguide Capillary Cell. Detailed descriptions of the procedure can be found in Liu et al. (2014, 2015a); Zeng et al. (2020). Following Zeng et al. (2022), we combined this data with BC measurements from a single-particle soot photometer (Schwarz et al., 2006) and sizing information from the laser aerosol spectrometer, to reconstruct the absorption coefficient of the original particle ensemble and to estimate uncertainties ($\approx 30\,\%$) for the full measurement and analysis procedure.

The second comparison dataset is based on in situ PAS. The PAS instruments during FIREX-AQ provided real-time measurements of the dry aerosol absorption coefficient at wavelengths of 405, 532 and 664 nm. Given the low humidity conditions during the Shady fire ($< 35\,\%$), dry absorption can be considered representative of ambient absorption (Lan-

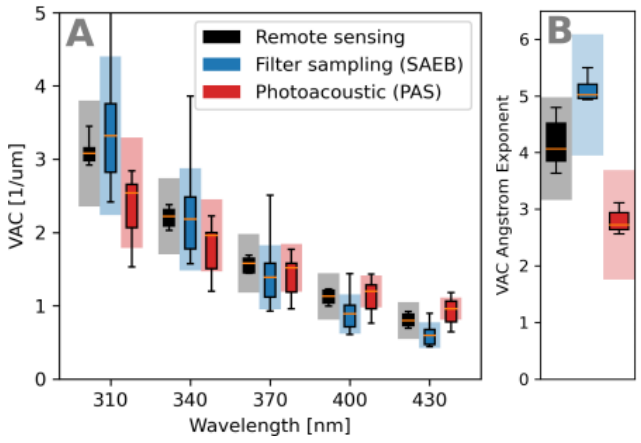


Figure 7. Statistical comparison of VACs from our retrieval with aircraft-based data from offline filter-based SAEB and in situ PAS measurements. Boxes expand from the first to the third quartile of the data. Whiskers indicate the 5th and 95th percentile. Grey shaded areas in the background indicate the retrieval's average propagated errors, including systematic uncertainties that are not necessarily reflected by the box plots. Blue and red shaded areas in the background indicate average specified uncertainties for the SAEB and PAS measurements, respectively.

gridge et al., 2013). In contrast to SAEB, PAS observations measure directly the total absorption of aerosol in its particulate state. Uncertainties for the direct PAS measurements are estimated to be 20 % (Langridge et al., 2011). However, since the measurements were limited to three wavelengths in the visible, UV absorption properties were determined as described in Zeng et al. (2022), a process based on log-linear spectral extrapolation, something that potentially introduces considerable biases (Liu et al., 2015b; Zeng et al., 2022).

Zeng et al. (2022) performed a detailed comparison of absorption coefficients from SAEB and PAS and reported substantial inconsistency (as also evident in Figs. 7 and S8 in the present study). In the following, we perform a similar comparison, this time including our remote sensing results. For this purpose, absorption coefficients from PAS and SAEB were converted to VACs, assuming the same aerosol PSDs from the laser aerosol spectrometer (Sect. 3.5) that were used in our retrieval. For 14 transects during the Shady fire, all three absorption datasets (Remote sensing, SAEB and PAS) contain sufficient data and enough temporal overlap for meaningful comparisons to be made. Comparing data for individual transects shows that, within the specified uncertainties, our remote sensing results agree with at least one of the aircraft-based comparison datasets for nearly all transects and wavelengths (Fig. S8).

Figure 7 summarizes this comparison over all transects in the form of VAC box-plots at five UV-Vis wavelengths and VAC Angstrom exponents, thereby revealing general systematic features. On average, our retrieved VACs and Angstrom coefficients are between the SAEB and PAS results. In the UV spectral range, VACs are closer to the SAEB data but stay slightly below, whereas in the visible, our results tend towards the PAS data. These trends agree well with the recent analysis by Zeng et al. (2022). In the UV, they expect the SAEB measurements to be most reliable, since soluble BrC dominates the absorption. At the same time, they postulate a potential overestimation in SAEB measurements due to the alteration of the chromophores through the extraction process, such as change in pH or direct reaction with the solvent. The UV PAS measurements suffer from uncertainties introduced by the UV extrapolation. Since the Angstrom exponent is inferred in the visible, where BC weakens the absorption wavelength dependence, PAS is expected to increasingly underestimate the real VAC towards shorter wavelengths. The situation changes in the visible spectral range. Here, SAEB excludes potentially relevant absorption from insoluble compounds and thus underestimates the VAC, whereas the PAS provides direct reliable measurements. However, while our results confirm the assumptions by Zeng et al. (2022), it should be noted that the propagated errors of the retrieval (with a large systematic contribution from uncertainty in the fixed real RI) could allow for other outcomes and further measurements would be beneficial to increase confidence in the validity of the results.

Our remote sensing results feature remarkably low variability (cf. small box sizes in Fig. 7), which is about three times less than in the corresponding aircraft-based comparison datasets. As demonstrated in Fig. S9, this low variability is not artificially imposed by our filtering (Sect. 4.2) but likely related to the enhanced spatial averaging inherent to remote sensing. This indicates that aircraft-based comparison measurements averaged over a single plume transect may suffer from biases due to variations associated with the specific height at which the plume was probed and variability in the plume geometry during the transect. Therefore, these values are not necessarily representative for the entire plume cross-section. This effect may be in part responsible for the large variability in absorption properties reported in the literature, and for the current consensus that a simple parameterization of the aerosol absorption properties of BB cannot be found (Laskin et al., 2015).

4.4 Dependence on plume age

Based on the data from all three investigated fires, we find a dependence of imaginary RI, VAC and SSC on physical plume age (Figs. 8 and S10), with Pearson correlation coefficients of ≈ 0.5. Fitting an exponential decay to data of strongly absorbing wavelengths (308 to 347 nm), yields half-lives $\tau_{1/2}$ of 13 ± 3, 16 ± 4 and 17 ± 4 h for imaginary RI, VAC and SSC, respectively. The fit result for VAC is indicated by the gray dashed line in Fig. 8. The values obtained are in good agreement with previous studies investigating the oxidative and photochemical bleaching of BB aerosol (which leads to a decay of BrC absorption with plume age).

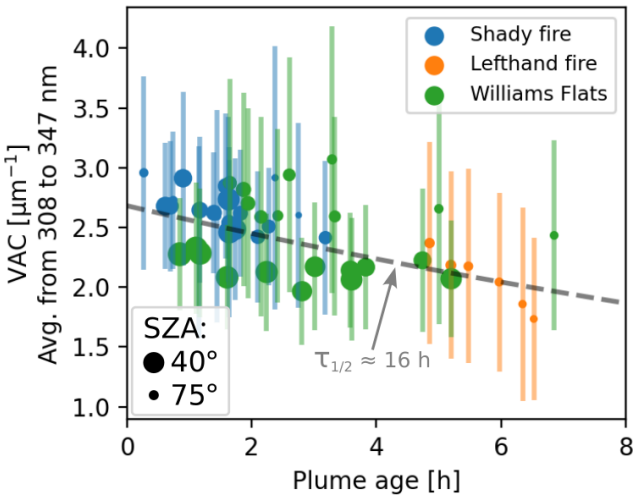


Figure 8. The dependence of the volume absorption cross-section (averaged from 308 to 347 nm) on plume age is shown for the three fires, which burned under similar conditions in similar ecosystems (Pearson correlation coefficient 0.5). Similar plots for the imaginary RI and SSC can be found in Supplement Fig. S10. Error bars represent propagated errors. Marker size indicates cos(SZA), as a proxy for the solar exposure. The grey dashed line shows an exponential fit, based on all data points.

While laboratory studies with synthetic organic aerosol have reported a wide range of absorption half-lives from a few minutes to several hours (Zhong and Jang, 2011; Zhao et al., 2015), measurements in real plumes report values between 9 and 24 h (Wang et al., 2016; Lee et al., 2014; Forrister et al., 2015; Zeng et al., 2022). Given the limited amount of data and the relatively large uncertainties, we could not identify a dependence of $\tau_{1/2}$ on the exposure to sunlight in terms of solar zenith angle (dot size in Fig. 8).

4.5 Variability among fires

Given the uncertainty limits in our retrievals, we find no significant differences in imaginary RI, VAC and SSA between the three fires (Fig. 9). This is surprising considering that aerosol absorption properties have been reported to vary significantly between different fires for a variety of reasons (Sect. 1). The small differences might be partly explained by the similarity in combustion conditions. A common proxy for combustion conditions is the modified combustion efficiency (MCE), defined as $\Delta CO_2/(\Delta CO + \Delta CO_2)$, where ΔCO and ΔCO_2 are background-corrected concentrations of carbon monoxide and carbon dioxide, respectively (Akagi et al., 2011). For both the Shady and the Williams Flats fires we find little variation in MCE throughout the plumes and average values close to 0.9 (see Table 1), representing approximately equal contributions from flaming and smoldering combustion (Stockwell et al., 2014). For the Lefthand fire, the enhancement ΔCO is too small to calculate a reliable MCE value.

Table 4. Values of various absorption properties and their uncertainties, with their wavelength and plume age dependencies.

	Property	A_0[a]	α	$\tau_{1/2}$
Values	k	0.023	3.5	13 h
	VAC	1.1 μm^{-1}	4.0	16 h
	SSC	0.1	2.9	17 h
Uncertainties	k	0.0068	3.5	NA
	VAC	0.32 μm^{-1}	3.2	NA
	SSC	0.028	2.3	NA

[a] Property value at wavelength $\lambda_0 = 400$ nm and plume age $t = 0$ h.

4.6 Parameterization for general applications

We have seen that the aerosol UV absorption properties depend on wavelength and plume age, while the variation among the three investigated fires is insignificant within the retrieval uncertainties. Our retrieved absorption properties might therefore be applicable to other fires, for which comprehensive measurements similar to FIREX-AQ are not available. Example applications are chemical transport modeling, assessment of BB radiative forcing, or other remote sensing applications such as trace gas retrievals from satellite-based measurements. For such purposes we consolidate our results into a parameterization, that considers the relevant dependencies according to:

$$A(\lambda, t) = A_0 \cdot \left(\frac{\lambda_0}{\lambda}\right)^{\alpha} \cdot \exp\left(-\frac{t \ln 2}{\tau_{1/2}}\right). \quad (13)$$

$A(\lambda, t)$ is the absorption property of interest (either k, VAC or SSC), that is a function of wavelength λ and physical smoke age t. A_0 is the value of the property at $\lambda_0 = 400$ nm and $t = 0$ h. The wavelength parameterization is given by an Angstrom dependence with exponent α, while plume age is characterized by an exponential decay with half-life $\tau_{1/2}$. Table 4 provides the values for A_0, α and τ for each absorption property. These values were determined by fitting Eq. 13 to correspondingly binned averages of our retrieval results. It should be pointed out that this parameterization is intended for plume ages between 0.5 and 8 h, and a wavelength range from 308 to 440 nm; it is probably only valid for fires with fuel and MCE values similar to those for the three fires treated in the present study (see Table 1).

5 Conclusions

Remote sensing based on radiation measurements taken inside and in proximity of BB plumes is a promising approach to determine aerosol UV absorption properties in a contact-

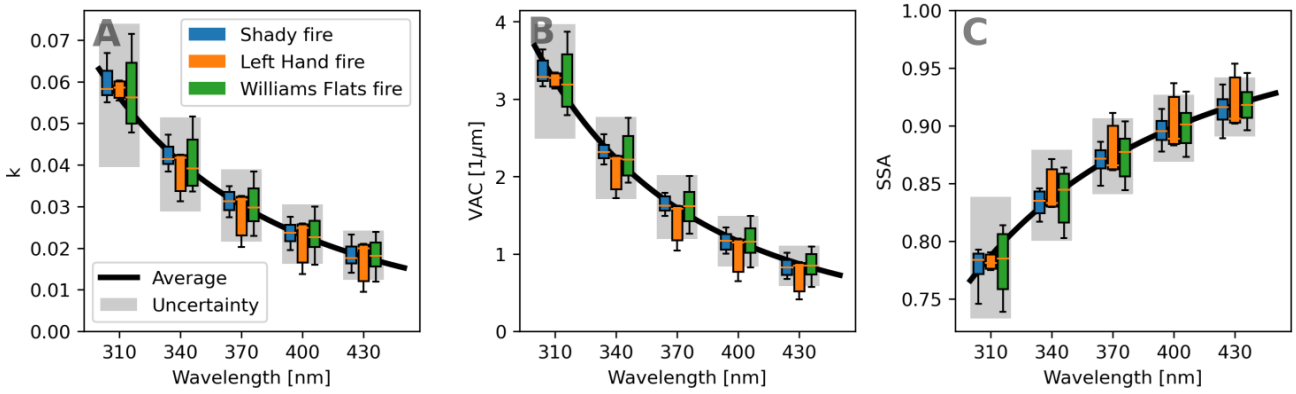


Figure 9. Statistical comparison of retrieved spectral imaginary RI, VAC and SSA for the three investigated fires. The plotted data have been adjusted to represent a plume-age of zero, using the plume age parameterization described in Sect. 4.6. Boxes expand from the first to the third quartile of the data. Whiskers indicate the 5th and 95th percentiles. Surprisingly, the results for different fires agree within the retrieval uncertainties.

less manner. Using the VPC radiative transfer model, we developed a retrieval scheme based on actinic fluxes, including a rigorous error propagation scheme that considers various sources of uncertainties. This retrieval was applied to three fires from the FIREX-AQ campaign.

The success and quality of the retrieval results clearly depends on the geometrical configurations and the atmospheric conditions for a given fire scenario. Best results are achieved at high sun (SZA $< 75°$) and when the aircraft is inside a plume of moderate AOD (between 1 and 3 at 532 nm) with little horizontal variability. Under such favorable conditions, the results and uncertainty estimates are stable and consistent. Propagated uncertainties for the retrieved imaginary RI, VAC and SSC are on the order of 20 % to 30 %. Uncertainties in the Angstrom exponent for the imaginary RI are $< 20\,\%$. Less favorable conditions can destabilize the retrieval, leading to unrealistic results and false uncertainty estimates. This was the case for $\approx 20\,\%$ of the retrievals performed in the present study, which could be identified and filtered based on simple criteria. For the remaining data, we find a relatively small variability of aerosol absorption properties within individual transects on the order of or smaller than the retrieval uncertainties. We conclude that BB particle properties are surprisingly homogeneous for smoke from the same fire and of similar atmospheric age, at least on the scales of the retrieval spatial resolution (few km horizontally, few hundred meters vertically). Under favorable conditions, the error of the retrieval is dominated by uncertainties in the real RI and the plume AOD, whereas the aerosol size distribution is a minor contributor. This is particularly interesting for aerosol absorption remote sensing of other plumes, where comprehensive additional measurements such as those obtained during FIREX-AQ are not available. Actinic fluxes have been and likely will be measured routinely during aircraft campaigns that comprise BB plume events, such as ARCTAS (Corr et al., 2012) SEAC4RS (Wolfe et al., 2022), WE-CAN (e.g. Palm et al., 2021; Peng et al., 2021), or ASIA-AQ (Zavaleta and Vasques). In the future, our evaluation scheme might be extended to such datasets, to cover a wider range of fire scenarios. Furthermore, the retrieval scheme can be modified for application to additional measured quantities, such as radiance spectra, and to other geometries, e.g., from ground or space.

Our forward model uses a Mie code to map microphysical properties (size distribution and complex refractive index) to optical bulk properties (extinction, single-scattering albedo, and phase function (see Sect. 3.2). This approach assumes an ensemble of homogeneous, spherical particles. Consequently, the retrieved imaginary refractive index (RI) should be interpreted as a "Mie-equivalent" value. It may thus diverge from the physical RI of the actual particles, but remains radiatively consistent, in the sense that the Mie code will yield optical bulk properties that are close to reality. Furthermore, we parameterize the spectral dependence of all retrieved variables using a simple Angstrom relationship. While our fit residuals (see Fig. S6) suggest this representation is robust within the scope of our retrieval, caution is advised when extrapolating these spectral dependencies beyond the wavelength range investigated in this work.

We gained new insights into the validity and limitations of coincident aircraft-based comparison measurements, including in situ photoacoustic spectroscopy (PAS) and offline filter-sampling analysis (SAEB). In the UV, we find closer agreement with the SAEB observations, while in the visible, our results show better agreement with the PAS measurements. This is in line with current speculations on the origin of the disagreement between the methods (e.g. Zeng et al., 2022). When comparing data for different transects, our retrieval results show about three times less variability than is the case with the corresponding aircraft-based comparison datasets. This illustrates the advantage inherent in the use of spatial averaging typical of remote sensing applica-

tions. In contrast to remote sensing observations, it seems that aircraft-based comparison measurements, averaged over a single plume transect, do not necessarily provide aerosol absorption properties that are representative of the entire plume cross-section. This effect may have contributed to the high variability of reported BB aerosol absorption in the past.

In the wavelength range between 308 and 440 nm, the retrievals yield average Angstrom coefficients of 3.5, 4.0, and 2.9 for the imaginary refractive index, VAC, and SSC, respectively. Between individual transects, the corresponding coefficients vary by about ± 0.5 (standard deviation), which is within the propagated retrieval uncertainty. In addition to this wavelength dependence, we also find a significant correlation with physical smoke age. For the smoke age range covered in the present study (0.5 to 8 h), we estimate a half-life decay time for the imaginary RI in the UV of 13 ± 3 h, and similar values for VAC and SSC. This is in agreement with other studies suggesting a limited lifetime for BrC (see Sect. 4.4). Encouraged by these findings, we have consolidated our results into a parameterization for aerosol absorption properties (Sect. 4.6), applicable to other fires with similar fuel, combustion states, and atmospheric conditions (Table 1), such as those generally found in the western US. Conceivable applications in this context are, for instance, plume chemistry models, chemical transport models, or trace gas remote sensing from satellite observations.

Appendix A: List of abbreviations

AOD	Aerosol optical depth
BB	Biomass burning
BC	Black carbon
BrC	Brown carbon
CAFS	CCD Actinic Flux Spectro-radiometer
FWHM	Full width at half maximum
PSD	Particle size distribution
RMSD	Root-mean-square deviation
RI	Refractive index
SAEB	Spectral analysis of extracted BrC chromophores
SSA	Single scattering albedo
SSC	Single scattering co-albedo (1-SSA)
SZA	Solar zenith angle
UV	Ultraviolet (spectral range)
VAC	Volume absorption cross-section
Vis	Visible (spectral range)
VPC	VLIDORT for photochemistry

Code and data availability. The raw data from the FIREX-AQ campaign is available on the "NASA Airborne Science Data for Atmospheric Composition" database: https://www-air.larc.nasa.gov/cgi-bin/ArcView/firexaq (last access: 23 October 2026). The latest version of the VPC model is on a private Github repository. The authors can provide access on request. The retrieval code and raw results are available from the authors on request.

Supplement. The supplement related to this article is available online at https://doi.org/10.5194/acp-26-15423-2026-supplement.

Author contributions. JLT developed and applied the retrieval scheme, evaluated the data and wrote the first draft of the manuscript. NB and SFC provided the basis for this work, by performing pilot studies and driving the expansion of the VLIDORT-QS Fortran code written by RS and MC for its use in VPC and the retrieval framework. SH and KU collected and processed the CAFS data and advised on its assimilation in the study. VN and NT advised on radiative transfer, inversion and information content aspects of this work. JH and TS collected and processed the lidar profiles and advised on their assimilation in the study. RW, RZ and JD collected and processed the SAEB data, advised on its assimilation in the study and supported the comparison of retrieval and aircraft-based measurement methods. RM and EW collected and processed data from the TSI Laser Aerosol Spectrometer, the PSAP and the Nephelometer. JS initiated the investigations and contributed to all project activities as the principal investigator. All authors contributed to the manuscript.

Competing interests. The contact author has declared that none of the authors has any competing interests.

Disclaimer. Publisher's note: Copernicus Publications remains neutral with regard to jurisdictional claims made in the text, published maps, institutional affiliations, or any other geographical representation in this paper. The authors bear the ultimate responsibility for providing appropriate place names. Views expressed in the text are those of the authors and do not necessarily reflect the views of the publisher.

Acknowledgements. SH and KU are supported by the NSF National Center for Atmospheric Research, which is a major facility sponsored by the U.S. National Science Foundation under Cooperative Agreement No. 1852977. Part of this research was carried out at the Jet Propulsion Laboratory, California Institute of Technology. We acknowledge the FIREX-AQ PIs Glenn Diskin (DACOM) and Nick Wagner (NOAA AOP) for providing their data. We acknowledge the free use of the TROPOMI surface DLER database provided through the Sentinel-5p+ Innovation project of the European Space Agency (ESA). The TROPOMI surface DLER database was created by the Royal Netherlands Meteorological Institute (KNMI).

Financial support. This research has been supported by the National Oceanic and Atmospheric Administration (grant no. NA17OAR4310005) and the National Aeronautics and Space Administration (grant nos. 80NSSC21K1447, 80NSSC18K0662, 80NSSC18K0631, 80NSSC18K0638, 80NSSC21K1446, 80NSSC25K0017, and 80NM0018D0004).

Review statement. This paper was edited by Jason Cohen and reviewed by three anonymous referees.

References

Ajtai, T., Filep, Á., Schnaiter, M., Linke, C., Vragel, M., Bozóki, Z., Szabó, G., and Leisner, T.: A novel multi−wavelength photoacoustic spectrometer for the measurement of the UV–vis–NIR spectral absorption coefficient of atmospheric aerosols, J. Aerosol Sci., 41, 1020–1029, https://doi.org/10.1016/j.jaerosci.2010.07.008, 2010.

Akagi, S. K., Yokelson, R. J., Wiedinmyer, C., Alvarado, M. J., Reid, J. S., Karl, T., Crounse, J. D., and Wennberg, P. O.: Emission factors for open and domestic biomass burning for use in atmospheric models, Atmos. Chem. Phys., 11, 4039–4072, https://doi.org/10.5194/acp-11-4039-2011, 2011.

Aknan, A. and Chen, G.: NASA Airborne Science Data for Atmospheric Composition, FIREX-AQ Data Repository, https://www-air.larc.nasa.gov/missions/firex-aq/ (last access: 23 October 2026), 2023.

Arnott, P. W., Moosmüller, H., Fred Rogers, C., Jin, T., and Bruch, R.: Photoacoustic spectrometer for measuring light absorption by aerosol: instrument description, Atmos. Environ., 33, 2845–2852, https://doi.org/10.1016/S1352-2310(98)00361-6, 1999.

Barbaro, E., De Arellano, J. V., Ouwersloot, H. G., Schröter, J. S., Donovan, D. P., and Krol, M. C.: Aerosols in the convective boundary layer: Shortwave radiation effects on the coupled land-atmosphere system, J. Geophys. Res.: Atmos., 119, 5845–5863, https://doi.org/10.1002/2013JD021237, 2014.

Barnard, J. C., Volkamer, R., and Kassianov, E. I.: Estimation of the mass absorption cross section of the organic carbon component of aerosols in the Mexico City Metropolitan Area, Atmos. Chem. Phys., 8, 6665–6679, https://doi.org/10.5194/acp-8-6665-2008, 2008.

Beck, H. A., Niessner, R., and Haisch, C.: Development and characterization of a mobile photoacoustic sensor for on-line soot emission monitoring in diesel exhaust gas, Anal. Bioanal. Chem., 375, 1136–1143, https://doi.org/10.1007/s00216-003-1810-8, 2003.

Bhartia, P. K.: OMI/Aura Ozone (O_3) Total Column 1-Orbit L2 Swath 13×24 km, NASA Goddard Earth Sciences Data, https://doi.org/10.5067/AURA/OMI/DATA2024, 2012.

Bohren, C. F. and Huffman, D. R.: Absorption and Scattering of Light by Small Particles, Wiley, 1 edn., ISBN 978-0-471-29340-8, https://doi.org/10.1002/9783527618156, 1998.

Bond, T. C. and Bergstrom, R. W.: Light Absorption by Carbonaceous Particles: An Investigative Review, Aerosol Sci. Technol., 40, 27–67, https://doi.org/10.1080/02786820500421521, 2006.

Bond, T. C., Streets, D. G., Yarber, K. F., Nelson, S. M., Woo, J., and Klimont, Z.: A technology-based global inventory of black and organic carbon emissions from combustion, J. Geophys. Res.: Atmos., 109, 2003JD003697, https://doi.org/10.1029/2003JD003697, 2004.

Bond, T. C., Habib, G., and Bergstrom, R. W.: Limitations in the enhancement of visible light absorption due to mixing state, J. Geophys. Res.: Atmos., 111, 2006JD007315, https://doi.org/10.1029/2006JD007315, 2006.

Bousserez, N.: Space-based retrieval of NO2 over biomass burning regions: quantifying and reducing uncertainties, Atmos. Meas. Tech., 7, 3431–3444, https://doi.org/10.5194/amt-7-3431-2014, 2014.

Browell, E.: Differential absorption lidar sensing of ozone, Proceedings of the IEEE, 77, 419–432, https://doi.org/10.1109/5.24128, 1989.

Cappa, C. D., Lack, D. A., Burkholder, J. B., and Ravishankara, A. R.: Bias in Filter-Based Aerosol Light Absorption Measurements Due to Organic Aerosol Loading: Evidence from Laboratory Measurements, Aerosol Sci. Technol., 42, 1022–1032, https://doi.org/10.1080/02786820802389285, 2008.

Chakrabarty, R. K., Pervez, S., Chow, J. C., Watson, J. G., Dewangan, S., Robles, J., and Tian, G.: Funeral Pyres in South Asia: Brown Carbon Aerosol Emissions and Climate Impacts, Environ. Sci. Technol. Lett., 1, 44–48, https://doi.org/10.1021/ez4000669, 2014.

Chakrabarty, R. K., Shetty, N. J., Thind, A. S., Beeler, P., Sumlin, B. J., Zhang, C., Liu, P., Idrobo, J. C., Adachi, K., Wagner, N. L., Schwarz, J. P., Ahern, A., Sedlacek, A. J., Lambe, A., Daube, C., Lyu, M., Liu, C., Herndon, S., Onasch, T. B., and Mishra, R.: Shortwave absorption by wildfire smoke dominated by dark brown carbon, Nat. Geosci., 16, 683–688, https://doi.org/10.1038/s41561-023-01237-9, 2023.

Chang, K.-E., Hsiao, T.-C., Tsay, S.-C., Lin, T.-H., Griffith, S. M., Liu, C.-Y., and Chou, C. C. K.: Embedded information of aerosol type, hygroscopicity and scattering enhancement factor revealed by the relationship between PM_2.5 and aerosol optical depth, Sci. Tot. Environ., 867, 161471, https://doi.org/10.1016/j.scitotenv.2023.161471, 2023.

Cheng, Z., Atwi, K., Hajj, O. E., Ijeli, I., Fischer, D. A., Smith, G., and Saleh, R.: Discrepancies between brown carbon light-absorption properties retrieved from online and offline measurements, Aerosol Sci. Technol., 55, 92–103, https://doi.org/10.1080/02786826.2020.1820940, 2021.

Corr, C. A., Krotkov, N., Madronich, S., Slusser, J. R., Holben, B., Gao, W., Flynn, J., Lefer, B., and Kreidenweis, S. M.: Retrieval of aerosol single scattering albedo at ultraviolet wavelengths at the T1 site during MILAGRO, Atmos. Chem. Phys., 9, 5813–5827, https://doi.org/10.5194/acp-9-5813-2009, 2009.

Corr, C. A., Hall, S. R., Ullmann, K., Anderson, B. E., Beyersdorf, A. J., Thornhill, K. L., Cubison, M. J., Jimenez, J. L., Wisthaler, A., and Dibb, J. E.: Spectral absorption of biomass burning aerosol determined from retrieved single scattering albedo during ARCTAS, Atmos. Chem. Phys., 12, 10505–10518, https://doi.org/10.5194/acp-12-10505-2012, 2012.

Drinovec, L., Močnik, G., Zotter, P., Prévôt, A. S. H., Ruckstuhl, C., Coz, E., Rupakheti, M., Sciare, J., Müller, T., Wiedensohler, A., and Hansen, A. D. A.: The "dual-spot" Aethalometer: an improved measurement of aerosol black carbon with real-time loading compensation, Atmos. Meas. Tech., 8, 1965–1979, https://doi.org/10.5194/amt-8-1965-2015, 2015.

Drugé, T., Nabat, P., Mallet, M., Michou, M., Rémy, S., and Dubovik, O.: Modeling radiative and climatic effects of brown carbon aerosols with the ARPEGE-Climat global climate model, Atmos. Chem. Phys., 22, 12167–12205, https://doi.org/10.5194/acp-22-12167-2022, 2022.

Feng, Y., Ramanathan, V., and Kotamarthi, V. R.: Brown carbon: a significant atmospheric absorber of solar radiation?, Atmos. Chem. Phys., 13, 8607–8621, https://doi.org/10.5194/acp-13-8607-2013, 2013.

Fischer, D. A. and Smith, G. D.: A portable, four-wavelength, single-cell photoacoustic spectrometer for ambient aerosol absorption, Aerosol Sci. Technol., 52, 393–406, https://doi.org/10.1080/02786826.2017.1413231, 2018.

Forrister, H., Liu, J., Scheuer, E., Dibb, J., Ziemba, L., Thornhill, K. L., Anderson, B., Diskin, G., Perring, A. E., Schwarz, J. P., Campuzano-Jost, P., Day, D. A., Palm, B. B., Jimenez, J. L., Nenes, A., and Weber, R. J.: Evolution of brown carbon in wildfire plumes, Geophys. Res. Lett., 42, 4623–4630, https://doi.org/10.1002/2015GL063897, 2015.

Hair, J. W., Hostetler, C. A., Cook, A. L., Harper, D. B., Ferrare, R. A., Mack, T. L., Welch, W., Izquierdo, L. R., and Hovis, F. E.: Airborne High Spectral Resolution Lidar for profiling aerosol optical properties, Appl. Opt., 47, 6734, https://doi.org/10.1364/AO.47.006734, 2008.

Hall, S. R., Ullmann, K., Prather, M. J., Flynn, C. M., Murray, L. T., Fiore, A. M., Correa, G., Strode, S. A., Steenrod, S. D., Lamarque, J.-F., Guth, J., Josse, B., Flemming, J., Huijnen, V., Abraham, N. L., and Archibald, A. T.: Cloud impacts on photochemistry: building a climatology of photolysis rates from the Atmospheric Tomography mission, Atmos. Chem. Phys., 18, 16809–16828, https://doi.org/10.5194/acp-18-16809-2018, 2018.

Hecobian, A., Zhang, X., Zheng, M., Frank, N., Edgerton, E. S., and Weber, R. J.: Water-Soluble Organic Aerosol material and the light-absorption characteristics of aqueous extracts measured over the Southeastern United States, Atmos. Chem. Phys., 10, 5965–5977, https://doi.org/10.5194/acp-10-5965-2010, 2010.

Hodzic, A. and Duvel, J. P.: Impact of Biomass Burning Aerosols on the Diurnal Cycle of Convective Clouds and Precipitation Over a Tropical Island, J. Geophys. Res.: Atmos., 123, 1017–1036, https://doi.org/10.1002/2017JD027521, 2018.

Holmes, C. D., Schwarz, J. P., Fite, C. H., Agastra, A., Nowell, H. K., Ball, K., Bui, T. P., Dean-Day, J., Decker, Z. C. J., DiGagni, J. P., Diskin, G. S., Gargulinski, E. M., Halliday, H., Kondragunta, S., Nowak, J. B., Peterson, D. A., Robinson, M. A., Soja, A. J., Washenfelder, R. A., Xu, C., and Yokelson, R. J.: Age of smoke sampled by aircraft during FIREX-AQ: methods and critical evaluation, Earth Syst. Sci. Data Discuss. [preprint], https://doi.org/10.5194/essd-2025-307, in review, 2025.

Jeong, U., Tsay, S.-C., Hsu, N. C., Giles, D. M., Cooper, J. W., Lee, J., Swap, R. J., Holben, B. N., Butler, J. J., Wang, S.-H., Chantara, S., Hong, H., Kim, D., and Kim, J.: Simultaneous retrievals of biomass burning aerosols and trace gases from the ultraviolet to near-infrared over northern Thailand during the 2019 pre-monsoon season, Atmos. Chem. Phys., 22, 11957–11986, https://doi.org/10.5194/acp-22-11957-2022, 2022.

Jethva, H. and Torres, O.: Satellite-based evidence of wavelength-dependent aerosol absorption in biomass burning smoke inferred from Ozone Monitoring Instrument, Atmos. Chem. Phys., 11, 10541–10551, https://doi.org/10.5194/acp-11-10541-2011, 2011.

Kirchstetter, T. W., Novakov, T., and Hobbs, P. V.: Evidence that the spectral dependence of light absorption by aerosols is affected by organic carbon, J. Geophys. Res.: Atmos., 109, 2004JD004999, https://doi.org/10.1029/2004JD004999, 2004.

Kotchenruther, R. A. and Hobbs, P. V.: Humidification factors of aerosols from biomass burning in Brazil, J. Geophys. Res.: Atmos., 103, 32081–32089, https://doi.org/10.1029/98JD00340, 1998.

Krotkov, N. A., Bhartia, P. K., Herman, J. R., Slusser, J. R., Scott, G. R., Labow, G. J., Vasilkov, A. P., Eck, T., Doubovik, O., and Holben, B. N.: Aerosol ultraviolet absorption experiment (2002 to 2004), part 2: absorption optical thickness, refractive index, and single scattering albedo, Opt. Eng., 44, 1–17, https://doi.org/10.1117/1.1886819, 2005.

Lack, D. A., Cappa, C. D., Covert, D. S., Baynard, T., Massoli, P., Sierau, B., Bates, T. S., Quinn, P. K., Lovejoy, E. R., and Ravishankara, A. R.: Bias in Filter-Based Aerosol Light Absorption Measurements Due to Organic Aerosol Loading: Evidence from Ambient Measurements, Aerosol Sci. Technol., 42, 1033–1041, https://doi.org/10.1080/02786820802389277, 2008.

Lack, D. A., Richardson, M. S., Law, D., Langridge, J. M., Cappa, C. D., McLaughlin, R. J., and Murphy, D. M.: Aircraft Instrument for Comprehensive Characterization of Aerosol Optical Properties, Part 2: Black and Brown Carbon Absorption and Absorption Enhancement Measured with Photo Acoustic Spectroscopy, Aerosol Sci. Technol., 46, 555–568, https://doi.org/10.1080/02786826.2011.645955, 2012.

Laing, J. R., Jaffe, D. A., and Sedlacek III, A. J.: Comparison of Filter-based Absorption Measurements of Biomass Burning Aerosol and Background Aerosol at the Mt. Bachelor Observatory, Aerosol Air Qual. Res., 20, 663–678, https://doi.org/10.4209/aaqr.2019.06.0298, 2020.

Langridge, J. M., Richardson, M. S., Lack, D., Law, D., and Murphy, D. M.: Aircraft Instrument for Comprehensive Characterization of Aerosol Optical Properties, Part I: Wavelength-Dependent Optical Extinction and Its Relative Humidity Dependence Measured Using Cavity Ringdown Spectroscopy, Aerosol Sci. Technol., 45, 1305–1318, https://doi.org/10.1080/02786826.2011.592745, 2011.

Langridge, J. M., Richardson, M. S., Lack, D. A., Brock, C. A., and Murphy, D. M.: Limitations of the Photoacoustic Technique for Aerosol Absorption Measurement at High Relative Humidity, Aerosol Sci. Technol., 47, 1163–1173, https://doi.org/10.1080/02786826.2013.827324, 2013.

Laskin, A., Laskin, J., and Nizkorodov, S. A.: Chemistry of Atmospheric Brown Carbon, Chem. Rev., 115, 4335–4382, https://doi.org/10.1021/cr5006167, 2015.

Lee, H. J. J., Aiona, P. K., Laskin, A., Laskin, J., and Nizkorodov, S. A.: Effect of Solar Radiation on the Optical Properties and Molecular Composition of Laboratory Proxies of Atmospheric Brown Carbon, Environ. Sci. Technol., 48, 10217–10226, https://doi.org/10.1021/es502515r, 2014.

Levenberg, K.: A method for the solution of certain non-linear problems in least squares, Quart. Appl. Math., 2, 164–168, 1944.

Levoni, C., Cervino, M., Guzzi, R., and Torricella, F.: Atmospheric aerosol optical properties: a database of radiative characteristics for different components and classes, Appl. Opt., 36, 8031–8041, https://doi.org/10.1364/ao.36.008031, 1997.

Liu, D., Li, S., Hu, D., Kong, S., Cheng, Y., Wu, Y., Ding, S., Hu, K., Zheng, S., Yan, Q., Zheng, H., Zhao, D., Tian, P., Ye, J., Huang, M., and Ding, D.: Evolution of Aerosol Optical Properties from Wood Smoke in Real Atmosphere Influenced by Burning Phase and Solar Radiation, Environ. Sci. Technol., 55, 5677–5688, https://doi.org/10.1021/acs.est.0c07569, 2021.

Liu, J., Scheuer, E., Dibb, J., Ziemba, L. D., Thornhill, K. L., Anderson, B. E., Wisthaler, A., Mikoviny, T., Devi, J. J., Bergin, M., and Weber, R. J.: Brown carbon in the con-

tinental troposphere, Geophys. Res. Lett., 41, 2191–2195, https://doi.org/10.1002/2013GL058976, 2014.

Liu, J., Scheuer, E., Dibb, J., Diskin, G. S., Ziemba, L. D., Thornhill, K. L., Anderson, B. E., Wisthaler, A., Mikoviny, T., Devi, J. J., Bergin, M., Perring, A. E., Markovic, M. Z., Schwarz, J. P., Campuzano-Jost, P., Day, D. A., Jimenez, J. L., and Weber, R. J.: Brown carbon aerosol in the North American continental troposphere: sources, abundance, and radiative forcing, Atmos. Chem. Phys., 15, 7841–7858, https://doi.org/10.5194/acp-15-7841-2015, 2015a.

Liu, S., Aiken, A. C., Gorkowski, K., Dubey, M. K., Cappa, C. D., Williams, L. R., Herndon, S. C., Massoli, P., Fortner, E. C., Chhabra, P. S., Brooks, W. A., Onasch, T. B., Jayne, J. T., Worsnop, D. R., China, S., Sharma, N., Mazzoleni, C., Xu, L., Ng, N. L., Liu, D., Allan, J. D., Lee, J. D., Fleming, Z. L., Mohr, C., Zotter, P., Szidat, S., and Prévôt, A. S. H.: Enhanced light absorption by mixed source black and brown carbon particles in UK winter, Nat. Commun., 6, 8435, https://doi.org/10.1038/ncomms9435, 2015b.

Marquardt, D. W.: An algorithm for least-squares estimation of nonlinear parameters, J. Soc. Ind. Appl. Math., 11, 431–441, 1963.

Massoli, P., Murphy, D. M., Lack, D. A., Baynard, T., Brock, C. A., and Lovejoy, E. R.: Uncertainty in Light Scattering Measurements by TSI Nephelometer: Results from Laboratory Studies and Implications for Ambient Measurements, Aerosol Sci. Technol., 43, 1064–1074, https://doi.org/10.1080/02786820903156542, 2009.

Mok, J., Krotkov, N. A., Arola, A., Torres, O., Jethva, H., Andrade, M., Labow, G., Eck, T. F., Li, Z., Dickerson, R. R., Stenchikov, G. L., Osipov, S., and Ren, X.: Impacts of brown carbon from biomass burning on surface UV and ozone photochemistry in the Amazon Basin, Sci. Rep., 6, 36940, https://doi.org/10.1038/srep36940, 2016.

Moosmüller, H., Chakrabarty, R., and Arnott, W.: Aerosol light absorption and its measurement: A review, J. Quant. Spectrosc. Radiat. Transf., 110, 844–878, https://doi.org/10.1016/j.jqsrt.2009.02.035, 2009.

Palm, B. B., Peng, Q., Hall, S. R., Ullmann, K., Campos, T. L., Weinheimer, A., Montzka, D., Tyndall, G., Permar, W., Hu, L., Flocke, F., Fischer, E. V., and Thornton, J. A.: Spatially Resolved Photochemistry Impacts Emissions Estimates in Fresh Wildfire Plumes, Geophys. Res. Lett., 48, e2021GL095 443, https://doi.org/10.1029/2021GL095443, 2021.

Park, R. J., Kim, M. J., Jeong, J. I., Youn, D., and Kim, S.: A contribution of brown carbon aerosol to the aerosol light absorption and its radiative forcing in East Asia, Atmos. Environ., 44, 1414–1421, https://doi.org/10.1016/j.atmosenv.2010.01.042, 2010.

Peng, Q., Palm, B. B., Fredrickson, C. D., Lee, B. H., Hall, S. R., Ullmann, K., Campos, T., Weinheimer, A. J., Apel, E. C., Flocke, F., Permar, W., Hu, L., Garofalo, L. A., Pothier, M. A., Farmer, D. K., Ku, I.-T., Sullivan, A. P., Collett, J. L., Fischer, E., and Thornton, J. A.: Observations and Modeling of NO_x Photochemistry and Fate in Fresh Wildfire Plumes, ACS Earth Space Chem., 5, 2652–2667, https://doi.org/10.1021/acsearthspacechem.1c00086, 2021.

Petters, J. L., Saxena, V. K., Slusser, J. R., Wenny, B. N., and Madronich, S.: Aerosol single scattering albedo retrieved from measurements of surface UV irradiance and a radiative transfer model, J. Geophys. Res.: Atmos., 108, 2002JD002360, https://doi.org/10.1029/2002JD002360, 2003.

Pistone, K., Redemann, J., Doherty, S., Zuidema, P., Burton, S., Cairns, B., Cochrane, S., Ferrare, R., Flynn, C., Freitag, S., Howell, S. G., Kacenelenbogen, M., LeBlanc, S., Liu, X., Schmidt, K. S., Sedlacek III, A. J., Segal-Rozenhaimer, M., Shinozuka, Y., Stamnes, S., van Diedenhoven, B., Van Harten, G., and Xu, F.: Intercomparison of biomass burning aerosol optical properties from in situ and remote-sensing instruments in ORACLES-2016, Atmos. Chem. Phys., 19, 9181–9208, https://doi.org/10.5194/acp-19-9181-2019, 2019.

Pokhrel, R. P., Gordon, J., Fiddler, M. N., and Bililign, S.: Impact of combustion conditions on physical and morphological properties of biomass burning aerosol, Aerosol Sci. Technol., 55, 80–91, https://doi.org/10.1080/02786826.2020.1822512,2021.

Reid, J. S., Koppmann, R., Eck, T. F., and Eleuterio, D. P.: A review of biomass burning emissions part II: intensive physical properties of biomass burning particles, Atmos. Chem. Phys., 5, 799–825, https://doi.org/10.5194/acp-5-799-2005, 2005.

Rodgers, C. D.: Inverse Methods for Atmospheric Sounding: Theory and Practice, in: Series on Atmospheric, Oceanic and Planetary Physics, vol. 2, edited by: Taylor, F. W., https://doi.org/10.1142/3171, 2000.

Rowe, J. P., Zarzana, K. J., Kille, N., Borsdorff, T., Goudar, M., Lee, C. F., Koenig, T. K., Romero-Alvarez, J., Campos, T., Knote, C., Theys, N., Landgraf, J., and Volkamer, R.: Carbon Monoxide in Optically Thick Wildfire Smoke: Evaluating TROPOMI Using CU Airborne SOF Column Observations, ACS Earth Space Chem., 6, 1799–1812, https://doi.org/10.1021/acsearthspacechem.2c00048, 2022.

SAGE Science Team: SAGE II/ERBS Level 2 Solar Event Species Profiles Native Binary file – Version 7.0, NASA Goddard Earth Sciences Data and Information Services Center (GES DISC), https://doi.org/10.5067/ERBS/SAGEII/SOLAR_BINARY_L2-V7.0, 2012.

Saide, P. E., Thapa, L. H., Ye, X., Pagonis, D., Campuzano-Jost, P., Guo, H., Schuneman, M. L., Jimenez, J.-L., Moore, R., Wiggins, E., Winstead, E., Robinson, C., Thornhill, L., Sanchez, K., Wagner, N. L., Ahern, A., Katich, J. M., Perring, A. E., Schwarz, J. P., Lyu, M., Holmes, C. D., Hair, J. W., Fenn, M. A., and Shingler, T. J.: Understanding the Evolution of Smoke Mass Extinction Efficiency Using Field Campaign Measurements, Geophys. Res. Lett., 49, e2022GL099175, https://doi.org/10.1029/2022GL099175, 2022.

Schwarz, J. P., Gao, R. S., Fahey, D. W., Thomson, D. S., Watts, L. A., Wilson, J. C., Reeves, J. M., Darbeheshti, M., Baumgardner, D. G., Kok, G. L., Chung, S. H., Schulz, M., Hendricks, J., Lauer, A., Kärcher, B., Slowik, J. G., Rosenlof, K. H., Thompson, T. L., Langford, A. O., Loewenstein, M., and Aikin, K. C.: Single-particle measurements of midlatitude black carbon and light-scattering aerosols from the boundary layer to the lower stratosphere, J. Geophys. Res.: Atmos., 111, https://doi.org/10.1029/2006JD007076, 2006.

Shamjad, P. M., Satish, R. V., Thamban, N. M., Rastogi, N., and Tripathi, S. N.: Absorbing Refractive Index and Direct Radiative Forcing of Atmospheric Brown Carbon over Gangetic Plain, ACS Earth Space Chem., 2, 31–37, https://doi.org/10.1021/acsearthspacechem.7b00074, 2018.

Sharma, N., Arnold, I. J., Moosmüller, H., Arnott, W. P., and Mazzoleni, C.: Photoacoustic and nephelometric spectroscopy of aerosol optical properties with a supercontinuum light source, Atmos. Meas. Tech., 6, 3501–3513, https://doi.org/10.5194/amt-6-3501-2013, 2013.

Shetter, R. E. and Müller, M.: Photolysis frequency measurements using actinic flux spectroradiometry during the PEM-Tropics mission: Instrumentation description and some results, J. Geophys. Res.: Atmos., 104, 5647–5661, https://doi.org/10.1029/98JD01381, 1999.

Shetty, N. J., Pandey, A., Baker, S., Hao, W. M., and Chakrabarty, R. K.: Measuring light absorption by freshly emitted organic aerosols: optical artifacts in traditional solvent-extraction-based methods, Atmos. Chem. Phys., 19, 8817–8830, https://doi.org/10.5194/acp-19-8817-2019, 2019.

Shetty, N., Liu, P., Liang, Y., Sumlin, B., Daube, C., Herndon, S., Goldstein, A. H., and Chakrabarty, R. K.: Brown carbon absorptivity in fresh wildfire smoke: associations with volatility and chemical compound groups, Environ. Sci: Atmos., 3, 1262–1271, https://doi.org/10.1039/D3EA00067B, 2023.

Singh, S., Fiddler, M. N., and Bililign, S.: Measurement of size-dependent single scattering albedo of fresh biomass burning aerosols using the extinction-minus-scattering technique with a combination of cavity ring-down spectroscopy and nephelometry, Atmos. Chem. Phys., 16, 13491–13507, https://doi.org/10.5194/acp-16-13491-2016, 2016.

Spurr, R., Natraj, V., Colosimo, S., Stutz, J., Christi, M., and Korkin, S.: VLIDORT-QS: A quasi-spherical vector radiative transfer model, J. Quant. Spectrosc. Radiat. Transf., 291, 108341, https://doi.org/10.1016/j.jqsrt.2022.108341, 2022.

Stein, A. F., Draxler, R. R., Rolph, G. D., Stunder, B. J. B., Cohen, M. D., and Ngan, F.: NOAA's HYSPLIT Atmospheric Transport and Dispersion Modeling System, Bull. Am. Meteorol. Soc., 96, 2059–2077, https://doi.org/10.1175/BAMS-D-14-00110.1, 2015.

Stevens, R. and Dastoor, A.: A Review of the Representation of Aerosol Mixing State in Atmospheric Models, Atmosphere, 10, 168, https://doi.org/10.3390/atmos10040168, 2019.

Stockwell, C. E., Yokelson, R. J., Kreidenweis, S. M., Robinson, A. L., DeMott, P. J., Sullivan, R. C., Reardon, J., Ryan, K. C., Griffith, D. W. T., and Stevens, L.: Trace gas emissions from combustion of peat, crop residue, domestic biofuels, grasses, and other fuels: configuration and Fourier transform infrared (FTIR) component of the fourth Fire Lab at Missoula Experiment (FLAME-4), Atmos. Chem. Phys., 14, 9727–9754, https://doi.org/10.5194/acp-14-9727-2014, 2014.

Strutz, T.: Data fitting and uncertainty: a practical introduction to weighted least squares and beyond, Vieweg + Teubner, Wiesbaden, 1. aufl edn., ISBN 978-3-8348-1022-9, 2011.

Sumlin, B. J., Pandey, A., Walker, M. J., Pattison, R. S., Williams, B. J., and Chakrabarty, R. K.: Atmospheric Photooxidation Diminishes Light Absorption by Primary Brown Carbon Aerosol from Biomass Burning, Environ. Sci. Technol. Lett., 4, 540–545, https://doi.org/10.1021/acs.estlett.7b00393, 2017.

Sumlin, B. J., Heinson, Y. W., Shetty, N., Pandey, A., Pattison, R. S., Baker, S., Hao, W. M., and Chakrabarty, R. K.: UV–Vis–IR spectral complex refractive indices and optical properties of brown carbon aerosol from biomass burning, J. Quant. Spectrosc. Radiat. Transf., 206, 392–398, https://doi.org/10.1016/j.jqsrt.2017.12.009, 2018.

Sun, J., Zhang, Y., Zhi, G., Hitzenberger, R., Jin, W., Chen, Y., Wang, L., Tian, C., Li, Z., Chen, R., Xiao, W., Cheng, Y., Yang, W., Yao, L., Cao, Y., Huang, D., Qiu, Y., Xu, J., Xia, X., Yang, X., Zhang, X., Zong, Z., Song, Y., and Wu, C.: Brown carbon's emission factors and optical characteristics in household biomass burning: developing a novel algorithm for estimating the contribution of brown carbon, Atmos. Chem. Phys., 21, 2329–2341, https://doi.org/10.5194/acp-21-2329-2021, 2021.

Tellinghuisen, J.: Statistical Error Propagation, J. Phys. Chem. A, 105, 3917–3921, https://doi.org/10.1021/jp003484u, 2001.

Theys, N., Volkamer, R., Müller, J.-F., Zarzana, K. J., Kille, N., Clarisse, L., De Smedt, I., Lerot, C., Finkenzeller, H., Hendrick, F., Koenig, T. K., Lee, C. F., Knote, C., Yu, H., and Van Roozendael, M.: Global nitrous acid emissions and levels of regional oxidants enhanced by wildfires, Nat. Geosci. 13, 681–686, https://doi.org/10.1038/s41561-020-0637-7, 2020.

Theys, N., Yu, H., Franco, B., Clarisse, L., Volkamer, R., Cha, H., Kim, J., De Smedt, I., Stavrakou, T., van Gent, J., and Van Roozendael, M.: Atmospheric HONO Observed Over Global Biomass Burning Regions Using Satellite Observations of TROPOMI and GEMS, J. Geophys. Res.: Atmos., 130, e2024JD043 163, https://doi.org/10.1029/2024JD043163, 2025.

Tilstra, L. G., de Graaf, M., Trees, V. J. H., Litvinov, P., Dubovik, O., and Stammes, P.: A directional surface reflectance climatology determined from TROPOMI observations, Atmos. Meas. Tech., 17, 2235–2256, https://doi.org/10.5194/amt-17-2235-2024, 2024.

Tirpitz, J.-L., Colosimo, S. F., Brockway, N., Spurr, R., Christi, M., Hall, S., Ullmann, K., Hair, J., Shingler, T., Weber, R., Dibb, J., Moore, R., Wiggins, E., Natraj, V., Theys, N., and Stutz, J.: Modeling actinic flux and photolysis frequencies in dense biomass burning plumes, Atmos. Chem. Phys., 25, 1989–2015, https://doi.org/10.5194/acp-25-1989-2025, 2025.

Torres, O., Tanskanen, A., Veihelmann, B., Ahn, C., Braak, R., Bhartia, P. K., Veefkind, P., and Levelt, P.: Aerosols and surface UV products from Ozone Monitoring Instrument observations: An overview, J. Geophys. Res.: Atmos., 112, https://doi.org/10.1029/2007JD008809, 2007.

Virtanen, P., Gommers, R., Oliphant, T. E., Haberland, M., Reddy, T., Cournapeau, D., Burovski, E., Peterson, P., Weckesser, W., Bright, J., Van Der Walt, S. J., Brett, M., Wilson, J., Millman, K. J., Mayorov, N., Nelson, A. R. J., Jones, E., Kern, R., Larson, E., Carey, C. J., Polat, İ., Feng, Y., Moore, E. W., VanderPlas, J., Laxalde, D., Perktold, J., Cimrman, R., Henriksen, I., Quintero, E. A., Harris, C. R., Archibald, A. M., Ribeiro, A. H., Pedregosa, F., Van Mulbregt, P., SciPy 1.0 Contributors, Vijaykumar, A., Bardelli, A. P., Rothberg, A., Hilboll, A., Kloeckner, A., Scopatz, A., Lee, A., Rokem, A., Woods, C. N., Fulton, C., Masson, C., Häggström, C., Fitzgerald, C., Nicholson, D. A., Hagen, D. R., Pasechnik, D. V., Olivetti, E., Martin, E., Wieser, E., Silva, F., Lenders, F., Wilhelm, F., Young, G., Price, G. A., Ingold, G.-L., Allen, G. E., Lee, G. R., Audren, H., Probst, I., Dietrich, J. P., Silterra, J., Webber, J. T., Slavič, J., Nothman, J., Buchner, J., Kulick, J., Schönberger, J. L., De Miranda Cardoso, J. V., Reimer, J., Harrington, J., Rodríguez, J. L. C., Nunez-Iglesias, J., Kuczynski, J., Tritz, K., Thoma, M., Newville, M., Kümmerer, M., Bolingbroke, M., Tartre, M., Pak, M., Smith,

N. J., Nowaczyk, N., Shebanov, N., Pavlyk, O., Brodtkorb, P. A., Lee, P., McGibbon, R. T., Feldbauer, R., Lewis, S., Tygier, S., Sievert, S., Vigna, S., Peterson, S., More, S., Pudlik, T., Oshima, T., Pingel, T. J., Robitaille, T. P., Spura, T., Jones, T. R., Cera, T., Leslie, T., Zito, T., Krauss, T., Upadhyay, U., Halchenko, Y. O., and Vázquez-Baeza, Y.: SciPy 1.0: fundamental algorithms for scientific computing in Python, Nat. Methods, 17, 261–272, https://doi.org/10.1038/s41592-019-0686-2, 2020.

Wang, X., Heald, C. L., Ridley, D. A., Schwarz, J. P., Spackman, J. R., Perring, A. E., Coe, H., Liu, D., and Clarke, A. D.: Exploiting simultaneous observational constraints on mass and absorption to estimate the global direct radiative forcing of black carbon and brown carbon, Atmos. Chem. Phys., 14, 10989–11010, https://doi.org/10.5194/acp-14-10989-2014, 2014.

Wang, X., Heald, C. L., Sedlacek, A. J., de Sá, S. S., Martin, S. T., Alexander, M. L., Watson, T. B., Aiken, A. C., Springston, S. R., and Artaxo, P.: Deriving brown carbon from multiwavelength absorption measurements: method and application to AERONET and Aethalometer observations, Atmos. Chem. Phys., 16, 12733–12752, https://doi.org/10.5194/acp-16-12733-2016, 2016.

Warneke, C., Schwarz, J. P., Dibb, J., Kalashnikova, O., Frost, G., Al-Saad, J., Brown, S. S., Brewer, W. A., Soja, A., Seidel, F. C., Washenfelder, R. A., Wiggins, E. B., Moore, R. H., Anderson, B. E., Jordan, C., Yacovitch, T. I., Herndon, S. C., Liu, S., Kuwayama, T., Jaffe, D., Johnston, N., Selimovic, V., Yokelson, R., Giles, D. M., Holben, B. N., Goloub, P., Popovici, I., Trainer, M., Kumar, A., Pierce, R. B., Fahey, D., Roberts, J., Gargulinski, E. M., Peterson, D. A., Ye, X., Thapa, L. H., Saide, P. E., Fite, C. H., Holmes, C. D., Wang, S., Coggon, M. M., Decker, Z. C. J., Stockwell, C. E., Xu, L., Gkatzelis, G., Aikin, K., Lefer, B., Kaspari, J., Griffin, D., Zeng, L., Weber, R., Hastings, M., Chai, J., Wolfe, G. M., Hanisco, T. F., Liao, J., Campuzano Jost, P., Guo, H., Jimenez, J. L., Crawford, J., and The FIREX-AQ Science Team: Fire Influence on Regional to Global Environments and Air Quality (FIREX-AQ), J. Geophys. Res.: Atmos., 128, e2022JD037758, https://doi.org/10.1029/2022JD037758, 2023.

Weingartner, E., Saathoff, H., Schnaiter, M., Streit, N., Bitnar, B., and Baltensperger, U.: Absorption of light by soot particles: determination of the absorption coefficient by means of aethalometers, J. Aerosol Sci., 34, 1445–1463, https://doi.org/10.1016/S0021-8502(03)00359-8, 2003.

Wiegand, J. R., Mathews, L. D., and Smith, G. D.: A UV–Vis Photoacoustic Spectrophotometer, Anal. Chem., 86, 6049–6056, https://doi.org/10.1021/ac501196u, 2014.

Wolfe, G. M., Hanisco, T. F., Arkinson, H. L., Blake, D. R., Wisthaler, A., Mikoviny, T., Ryerson, T. B., Pollack, I., Peischl, J., Wennberg, P. O., Crounse, J. D., St. Clair, J. M., Teng, A., Huey, L. G., Liu, X., Fried, A., Weibring, P., Richter, D., Walega, J., Hall, S. R., Ullmann, K., Jimenez, J. L., Campuzano-Jost, P., Bui, T. P., Diskin, G., Podolske, J. R., Sachse, G., and Cohen, R. C.: Photochemical evolution of the 2013 California Rim Fire: synergistic impacts of reactive hydrocarbons and enhanced oxidants, Atmos. Chem. Phys., 22, 4253–4275, https://doi.org/10.5194/acp-22-4253-2022, 2022.

Wrana, F., von Savigny, C., Zalach, J., and Thomason, L. W.: Retrieval of stratospheric aerosol size distribution parameters using satellite solar occultation measurements at three wavelengths, Atmos. Meas. Tech., 14, 2345–2357, https://doi.org/10.5194/amt-14-2345-2021, 2021.

Xu, L., Crounse, J. D., Vasquez, K. T., Allen, H., Wennberg, P. O., Bourgeois, I., Brown, S. S., Campuzano-Jost, P., Coggon, M. M., Crawford, J. H., DiGangi, J. P., Diskin, G. S., Fried, A., Gargulinski, E. M., Gilman, J. B., Gkatzelis, G. I., Guo, H., Hair, J. W., Hall, S. R., Halliday, H. A., Hanisco, T. F., Hannun, R. A., Holmes, C. D., Huey, L. G., Jimenez, J. L., Lamplugh, A., Lee, Y. R., Liao, J., Lindaas, J., Neuman, J. A., Nowak, J. B., Peischl, J., Peterson, D. A., Piel, F., Richter, D., Rickly, P. S., Robinson, M. A., Rollins, A. W., Ryerson, T. B., Sekimoto, K., Selimovic, V., Shingler, T., Soja, A. J., St. Clair, J. M., Tanner, D. J., Ullmann, K., Veres, P. R., Walega, J., Warneke, C., Washenfelder, R. A., Weibring, P., Wisthaler, A., Wolfe, G. M., Womack, C. C., and Yokelson, R. J.: Ozone chemistry in western US wildfire plumes, Sci. Adv., 7, eabl3648, https://doi.org/10.1126/sciadv.abl3648, 2021.

Yu, H., Liu, S. C., and Dickinson, R. E.: Radiative effects of aerosols on the evolution of the atmospheric boundary layer, J. Geophys. Res.: Atmos., 107, https://doi.org/10.1029/2001JD000754, 2002.

Yuan, C., Zheng, J., Ma, Y., Jiang, Y., Li, Y., and Wang, Z.: Significant restructuring and light absorption enhancement of black carbon particles by ammonium nitrate coating, Environ. Pollu., 262, 114172, https://doi.org/10.1016/j.envpol.2020.114172, 2020.

Zavaleta, J. R. and Vasques, M.: Airborne and Satellite Investigation of Asian Air Quality (ASIA-AQ), https://espo.nasa.gov/asia-aq (last access: 23 October 2026), 2024.

Zeng, L., Zhang, A., Wang, Y., Wagner, N. L., Katich, J. M., Schwarz, J. P., Schill, G. P., Brock, C., Froyd, K. D., Murphy, D. M., Williamson, C. J., Kupc, A., Scheuer, E., Dibb, J., and Weber, R. J.: Global Measurements of Brown Carbon and Estimated Direct Radiative Effects, Geophys. Res. Lett., 47, e2020GL088747, https://doi.org/10.1029/2020GL088747, 2020.

Zeng, L., Dibb, J., Scheuer, E., Katich, J. M., Schwarz, J. P., Bourgeois, I., Peischl, J., Ryerson, T., Warneke, C., Perring, A. E., Diskin, G. S., DiGangi, J. P., Nowak, J. B., Moore, R. H., Wiggins, E. B., Pagonis, D., Guo, H., Campuzano-Jost, P., Jimenez, J. L., Xu, L., and Weber, R. J.: Characteristics and evolution of brown carbon in western United States wildfires, Atmos. Chem. Phys., 22, 8009–8036, https://doi.org/10.5194/acp-22-8009-2022, 2022.

Zhang, Y., Forrister, H., Liu, J., Dibb, J., Anderson, B., Schwarz, J. P., Perring, A. E., Jimenez, J. L., Campuzano-Jost, P., Wang, Y., Nenes, A., and Weber, R. J.: Top-of-atmosphere radiative forcing affected by brown carbon in the upper troposphere, Nat. Geosci., 10, 486–489, https://doi.org/10.1038/ngeo2960, 2017.

Zhao, R., Lee, A. K. Y., Huang, L., Li, X., Yang, F., and Abbatt, J. P. D.: Photochemical processing of aqueous atmospheric brown carbon, Atmos. Chem. Phys., 15, 6087–6100, https://doi.org/10.5194/acp-15-6087-2015, 2015.

Zhong, M. and Jang, M.: Light absorption coefficient measurement of SOA using a UV–Visible spectrometer connected with an integrating sphere, Atmos. Environ., 45, 4263–4271, https://doi.org/10.1016/j.atmosenv.2011.04.082, 2011.